SINGLE MOLECULE SUPER-RESOLUTION MICROSCOPY STUDY ON THE PRECISION WITH WHICH DNA NANOSTRUCTURES CAN ORIENT FLUORESCENT DYES

by

Brett Michael Ward

A dissertation
submitted in partial fulfillment
of the requirements for the degree of
Doctor of Philosophy in Materials Science and Engineering
Boise State University

August 2020

BOISE STATE UNIVERSITY GRADUATE COLLEGE

DEFENSE COMMITTEE AND FINAL READING APPROVALS

of the dissertation submitted by

Brett Michael Ward

Dissertation Title:	Single Molecule Super-Resolution Microscopy Study on thePrecision With Which DNA Nanostructures Can Orient Fluorescent Dyes
Date of Final Oral Examination:	11 June 2020

The following individuals read and discussed the dissertation submitted by student Brett Michael Ward, and they evaluated the presentation and response to questions during the final oral examination. They found that the student passed the final oral examination.

Elton Graugnard, Ph.D.	Chair, Supervisory Committee
William Knowlton, Ph.D.	Member, Supervisory Committee
Wan Kuang, Ph.D.	Member, Supervisory Committee
Matthew Ferguson, Ph.D.	Member, Supervisory Committee

The final reading approval of the dissertation was granted by Elton Graugnard, Ph.D., Chair of the Supervisory Committee. The dissertation was approved by the Graduate College.

DEDICATION

This work is dedicated to my parents and to my wife. The impact that your unwavering support and constant encouragement has had throughout this journey is impossible to measure.

ACKNOWLEDGMENTS

I have had the great fortune of watching both the Nano Materials and Devices Group and the Materials Science and Engineering graduate program at Boise State grow and change over the last eight years and in that time I have had the pleasure of meeting, learning from, and working with some great people. I would like to take this opportunity to acknowledge a few of the people that had a particularly positive influence on my graduate experience.

First, I would like to thank the members of my advisory committee, Dr. Knowlton, Dr. Kuang, and Dr. Ferguson for your guidance and feedback throughout this process. And to Dr. Gillespie for agreeing to serve as my Graduate Faculty Representative. I'd like to extend a very special thanks to my advisor, Dr. Graugnard, for giving me this opportunity and for challenging me every step along the way. Your patience, persistence, and ability to help me see the positives in any situation are the reasons I have made it to this point. Thank you.

I would also like to acknowledge the faculty and staff of the Micron School of Materials Science and Engineering who have kept me on track the past eight years, particularly Chad Watson, Stephanie Moran, and Jessica Economy who have helped me navigate the administrative side of this process with ease. I know I wasn't always the easiest student to help along and I thank you all for making everything outside of research go so smoothly. Also, a thank you to Dr. Hughes for taking every opportunity to offer a quick word of encouragement whenever our paths crossed.

Every past and present member of the NMDG research group has had an influence on this work but I'd like to acknowledge Paul Davis and Natalya Hallstrom for your instruction and guidance and for keeping the research labs running smoothly. Also, Chris Green, George Dickinson, Luca Piantanida, and Drew Lysne for training, advising, and working alongside me in the lab to support this work. There have been a few special people I've worked and learned alongside of who's impact on my graduate experience extend beyond the lab and so to Jackie Hodge, Brittany Kohoutek, and Michael Tobiason I would like to say thank you for making me socialize, creating an environment to relax and decompress, and providing the perfect balance of fun and focus which kept me on track throughout.

And finally, I'd like to thank everyone who reads this work. It means a lot to have someone take time from their day to hear what I have to share.

ABSTRACT

DNA nanotechnology enables the rapid, programmable self-assembly of novel structures and devices at the nanoscale. Utilizing the simplicity of Watson-Crick base pairing, DNA nanostructures are capable of assembling a variety of nanoparticles in arbitrary configurations with relative ease. Several emerging opto-electronic systems require a high degree of control of both the position and orientation of component fluorescent molecules, and while DNA nanostructures have demonstrated these capabilities, the precision with which DNA can orient fluorescent molecules is not well understood. Determining these bounds is critical in establishing the viability of DNA nanotechnology as a method of assembling fluorescent molecular networks.

In this work, using a combination of single molecule emission dipole imaging and super-resolution microscopy techniques, we correlate the orientations of fluorescent dye molecules to the orientations of their DNA substrates along five degrees of freedom. Several species of dyes were embedded within a DNA sequence using either one or two covalent tethers. These strands were incorporated directly into DNA origami structures to investigate the dependence of the location and binding architecture of the dye on the orientational precision of DNA nanostructures. Dye functionalized strands were also folded into a simpler four-arm junction, which was then immobilized on an origami structure to study the influence of the DNA substrate on dye orientation. Correlated analysis of super-resolution images of origami structures and single molecule emission dipole images from the embedded fluorescent molecule within the same structure allowed us to directly measure the relative orientations of dye molecules within DNA nanostructures. The resulting measurements revealed a moderate degree of polar angle control but a large variation in azimuthal control for the majority of structures examined. These measurements establish a single-molecule method for measurement of correlated orientations and provide a powerful approach for future studies on increasing the precision in the orientational control of fluorescent dye molecule monomers by DNA nanostructures.

TABLE OF CONTENTS

LIST OF TABLES

LIST OF FIGURES

LIST OF ABBREVIATIONS

°	degree
μL	Microliter
μm	Micrometer
2D	Two Dimensional
3D	Three Dimensional
4AJ	Four-Arm Junction
A	Adenine
Å	Angstrom
AFM	Atomic Force Microscope
AuNP	Gold Nanoparticle
bp	Base Pair
C	Cytosine
CCW	Counterclockwise
CHARMM	Chemistry at Harvard Macromolecular Mechanics
CPU	Central Processing Unit
Cryo-EM	Cryo-Electron Microscopy
CW	Continuous Wave
CW	Clockwise
Cy5	Cyanine 5
DARPA	Defense Advanced Research Projects Agency

deg	Degree
diIC2(5)	Non-Sulfonated Cyanine 5
diIC2(5)N	Single Tether Non-Sulfonated Cyanine 5
DNA	Deoxyribonucleic Acid
dsDNA	Dual Stranded DNA
EM	Electron-multiplier
EMCCD	Electron-multiplying CCD
ENRG MD	Elastic Network of Restraints Guided Molecular Dynamics
f	Azimuthal Angle
FOV	Field of View
FRET	Förster Resonance Energy Transfer
fs	Femtosecond
G	Guanine
GPU	Graphics Processing Unit
HPLC	High Performance Liquid Chromatography
kcal	Kilocalories
MFE	Minimum Free Energy
Mg	Magnesium
MgCl	Magnesium Chloride
MgHH	Magnesium Hexahydrate
mL	Milliliter
mM	Millimolar
mol	Mole

ms	Millisecond
n	Number of structures
NA	Numerical Aperture
NAMD	Nanoscale Molecular Dynamics
NHS	N-Hydroxysuccinimide
nm	Nanometer
nM	Nanomolar
ns	Nanosecond
NUPACK	Nucleic Acid Package
PAGE	Polyacrylamide Gel Electrophoresis
PAINT	Points Accumulation for Imaging in Nanoscale Topography
PCA	Protocatechuic Acid
PCD	Protocatechuate Dioxygenase
pM	Picomolar
PSF	Point Spread Function
q	Polar Angle
rcf	Relative Centrifugal Force
RHR	Right Hand Rule
ROI	Region of Interest
RT	Room Temperature
S/N	Signal to Noise Ratio
sm	Single Molecule
smSRM	Single Molecule Super-Resolution Microcroscopy

SP	Short Pass
SRM	Super-Resolution Microscopy
ssDNA	Single Stranded DNA
T	Thymine
TAE	Tris-Acetate-EDTA
TBE	Tris/Borate/EDTA
TEM	Transmission Electron Microscopy
TIRF	Total Internal Reflection Fluorescence
VMD	Visual Molecular Dynamics
λ	Wavelength

CHAPTER ONE: INTRODUCTION

As we reach the physical limits of the size and performance of traditional optoelectronic devices, efforts to move beyond the limits of classical physics are becoming more important[1]. One of the most significant goals of quantum mechanics research is the realization of a quantum computer, which could prove to be a significant stride forward in computing power but brings with it a number of challenges, namely that most current quantum computing devices require cryogenic temperatures for reliable operation[2,3]. Among the many possible methods of constructing a quantum computer, the use of photons as the carrier of information is emerging as a promising area of development[4]. Through careful control over the assembly of a system of nanoparticles, quantum devices could be built to perform a variety of functions analogous to traditional opto-electronics[5]. Using DNA as a template for assembling fluorescent dyes in such a manner has shown promising results with optical properties indicative of coherent energy transfer, as seen in Figure 1.1. However, these properties were observed in ensemble measurements[6], and the properties of individual assemblies of fluorescent dyes remain a mystery.

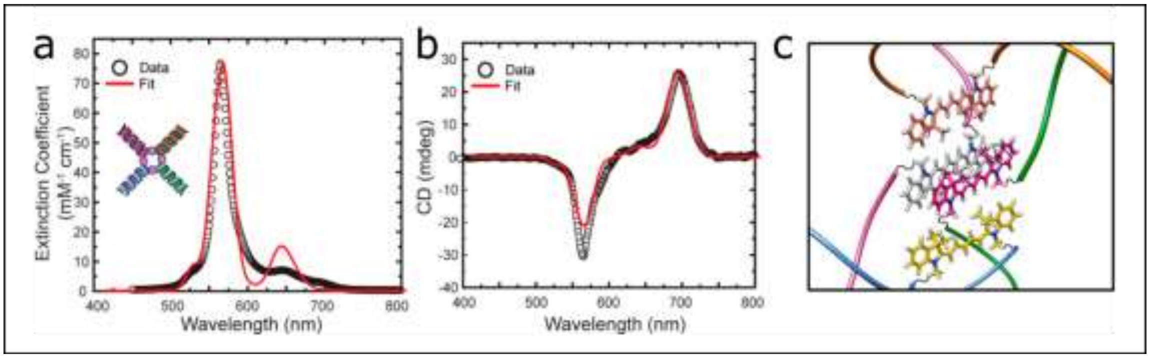

Figure 1.1: Optical spectra (a, b) and the deduced structures (c) of the DNA positioned dye aggregates responsible for them. The unique absorption and circular dichroism spectra depend on the number of dyes in an aggregate as well as their position and orientation relative to each other due to exciton delocalization. Ensemble measurements show that populations of DNA nanostructures have promise in positioning and orienting fluorescent molecules for optical networks. Figure adopted from Cannon, et al.[6]

Creating optically coherent networks is non-trivial, but like many engineering challenges, we can look to nature for a possible solution to the problem of positioning molecules to construct quantum devices that operate at ambient temperatures[7]. DNA nanotechnology offers a potentially ideal system for assembling such devices due to its size, addressability, dynamic properties and the number of seemingly identical structures that can be synthesized in parallel[8]. Coherent coupling of light between molecules is particularly sensitive to the relative orientations of the component particles, and while DNA has shown a high degree of control of positioning and orienting larger nanoparticles, its ability to orient fluorescent molecules structure to structure is less understood[9,10].

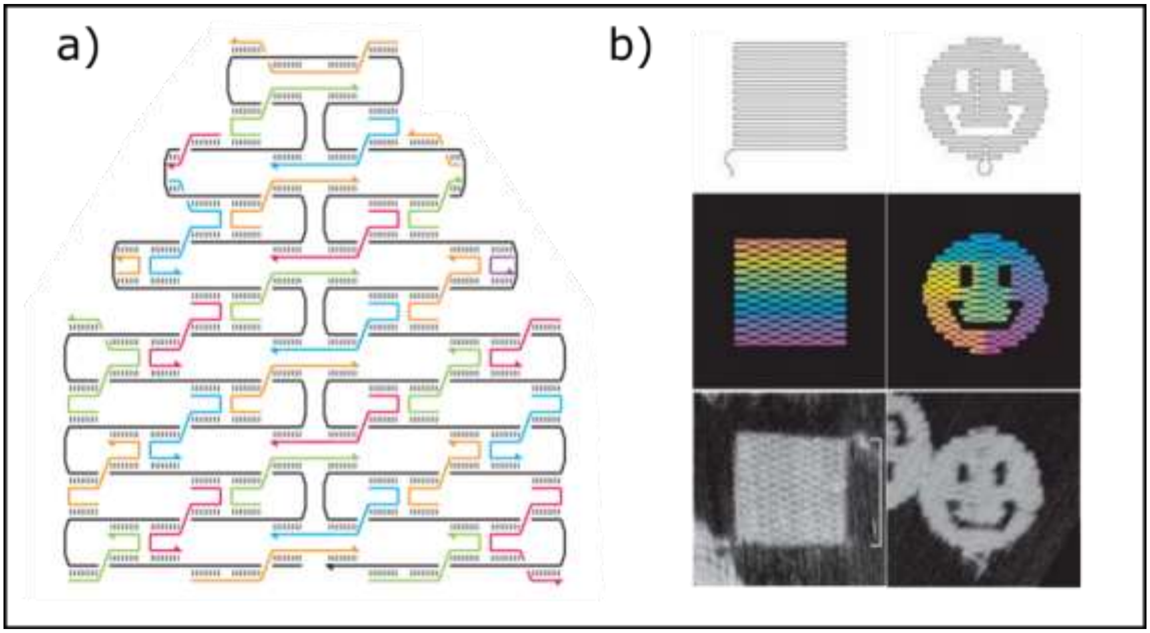

Figure 1.2: Schematic of DNA origami showing the design and resulting synthesized structures. a) A diagram showing the staple routing of a simple origami structure. The single scaffold strand (black) weaves through the entire structure, held in place by the short staple strands (multiple colors). Each staple strand contains multiple sequence domains that are complementary to specific locations on the scaffold strand. During folding these complementary domains hybridize together, pinning the scaffold in place. b) Two examples of possible origami patterns folded from the same scaffold strand sequence. The progression from design to modelling to synthesis shows how reproducible a DNA origami design can be in practice. Figure adopted from Rothemund[11].

Created in 1982 for the expressed purpose of positioning proteins, DNA nanotechnology has grown into a vast field of research reaching across many disciplines[12-15]. The introduction of DNA origami (illustrated in Figure 1.2), the folding of a long “scaffold” single-stranded DNA (ssDNA) through base-pairing to shorter “staple” ssDNA strands, which contain multiple sequence domains complementary to non-adjacent domains on the scaffold, further enhanced the functionality of DNA nanotechnology[11]. With the availability of design and modelling software, the ability to prototype potential structures serving specific needs is straight forward, and the necessary strands can be procured from a number of commercial vendors[16,17]. DNA origami allows for the positioning of a multitude of molecules and nanoparticles in arbitrary patterns, as seen the examples of Figure 1.3, and can serve as self-assembling device substrates[18-21].

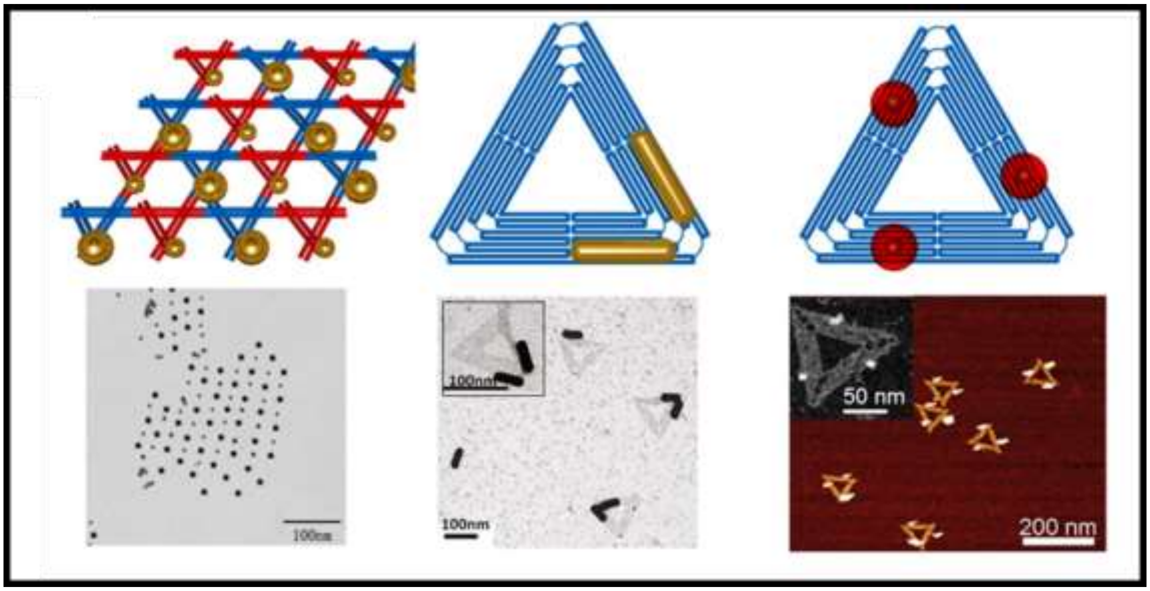

Figure 1.3: Examples of self-assembled DNA structures serving as templates for specific positioning and orientational control of nanoparticles. Top row shows schematics for DNA nanostructure (left) and DNA origami (middle, right) and the designed locations of immobilized nanoparticles. The bottom row shows experimental data of the same, confirming the positioning of the targets: left to right gold nanoparticles, gold nanorods, and quantum dots. Figure adopted from Zhang et al., https://pubs.acs.org/doi/10.1021/ja505101a[14]. Inquires and requests for permissions related to this figure should be directed to the American Chemical Society.

Due to the physical dimensions of DNA origami structures, typically 100 nm x 100 nm for M13mp18 scaffold-based origami, resolving single constructs in traditional optical microscopy is not possible. While structures can be imaged using techniques such as transmission electron microscopy (TEM) and atomic force microscopy (AFM) as in Figure 1.3, these techniques have low throughput. By fitting the point spread function (PSF) of a freely rotating single fluorescent molecule with a Gaussian distribution, the center of the PSF is measurable with a level of accuracy relative to the number of photons collected from that molecule[22]. If two fluorescent molecules are separated by a distance less than the diffraction limit of light, it is possible to resolve both molecules given enough time provided their photobleaching events occur in different integration periods[23]. Furthering this super resolution microscopy (SRM) technique, by exerting control over the on/off parameter (blinking) of the component fluorophores, one can resolve several dye locations below resolution limit of traditional optical microscopy[24-26].

In DNA origami, controlling the rate of blinking at specific sites and addressing specific locations is achievable through the technique of DNA points accumulation for imaging in nanoscale topography (DNA-PAINT)[27]. Therein, extended staple strands within the origami structure with specific ssDNA sequences create docking sites with which short, dye labeled imager strands in solution may interact. The arbitrary control over these docking site sequences creates locations that are addressable based on the imager strand or strands present in the imaging buffer, allowing multiple sites within a single structure to be resolved using a single imager dye on multiple sequences[28]. The benefit of such a system is the ability to perform multiplexed SRM imaging using a single fluorescent microscopy optical configuration with multiple washes.

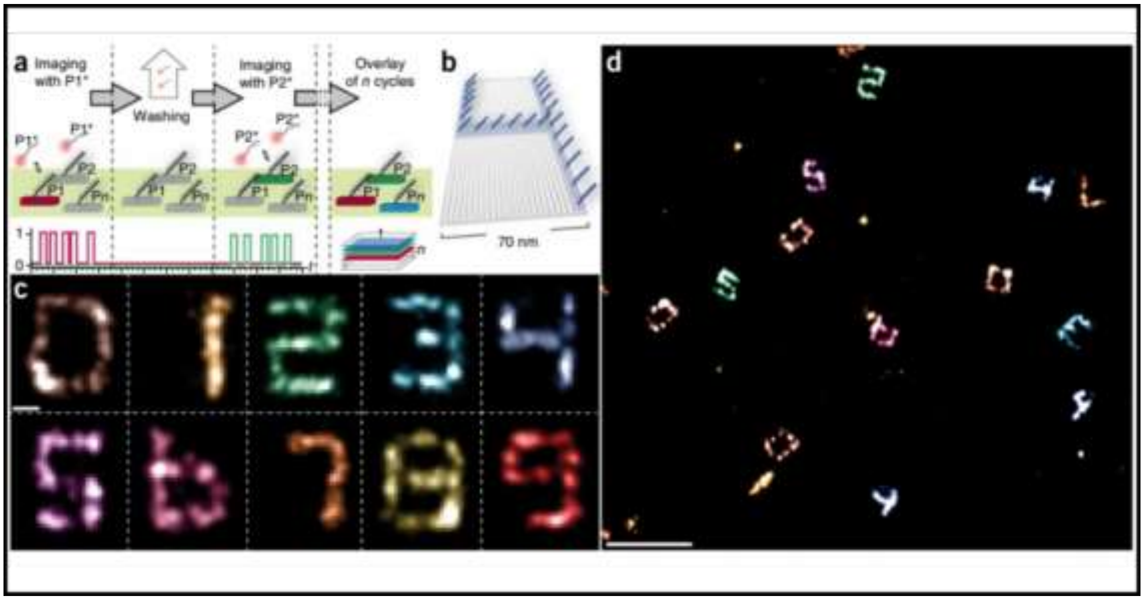

Figure 1.4: Illustration of DNA Exchange-PAINT. a) The steps necessary for multiplexed DNA-PAINT imaging. Each round of imaging is followed by a buffer rinse and introduction of a new imager solution meant to target different docking sites. b) An example of a DNA origami tile with a unique pattern of docking sites. c) Representative images of origami tiles resolved during the Exchange-PAINT process. Each number consists of multiple docking sites corresponding to a specific imager strand sequence. Blinking at these sites, and only at these sites, occurs when the exact complimentary imager sequence is present in the imaging buffer. d) A wide-field view of all ten overlaid SRM images showing the specificity of imager strand interactions without crosstalk between different origami substrates present on the surface. Figure adopted from Jungmann[28].

SRM image processing conventionally relies on the PSF from a single molecule exhibiting a Gaussian distribution, which is a reasonable approximation for dyes rotating freely on time scales much faster than image integration times but is less appropriate for dipoles fixed in space[29]. The PSF of a fixed dipole depends on the orientation of the molecule above the dielectric interface[30-33]. In single-molecule (sm) fluorescent microscopy, spreading these non-Gaussian PSFs over a sufficient number of camera pixels allows for the extraction of the component angles through pattern analysis algorithms, as seen in Figure 1.5 [34,35]. While dipole PSF pattern analysis and SRM each provide an important piece of information on the alignment of fluorescent molecules by a

DNA substrate, the complete system cannot be known without the direct correlation of the orientations of the substrate to the dipoles they are positioning.

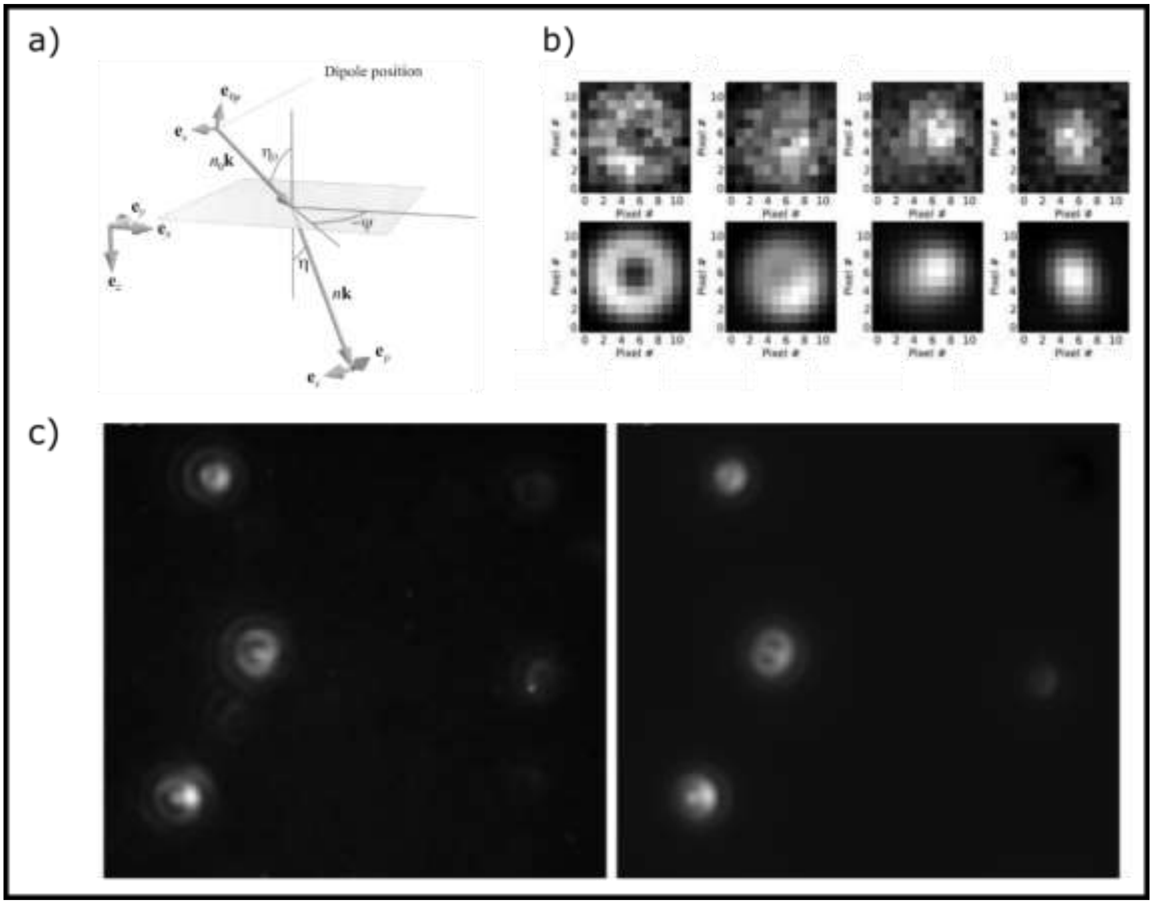

Figure 1.5: Single molecule imaging of fixed dipole emission patterns. a) The propagation of emitted photons across an interface. Emission is best described as system of standing plane waves with unique transmission components and incident angles. The resulting composite pattern beyond the interface is a superposition of all these waves. b) The real data (top) and the best fit simulated patterns (bottom) for individual observed single molecule dipole PSFs. c) A wide field image of observed Cy5-ssDNA dipole patterns (left) compared to the computed patterns (right). Each pattern is a result of the specific polar and azimuthal orientation of the dipole that produced it. Figure adapted from a) Böhmer[31] b) Mortensen[29], and c) Aguet[34].

The focus of this dissertation is to place upper and lower bounds on the precision to which single DNA constructs can orient single fluorescent molecules in a population through correlated single-molecule super-resolution microscopy (smSRM). The main body of this work is presented in Chapters Two and Three, which focus on measuring the orientations of several different single fluorescent dipoles positioned in various DNA constructs relative to their DNA substrates. Chapter Two focuses on dye molecules embedded into the double helix of a DNA origami structure with either one or two covalent bonds. The effects of position within the helix and the species of embedded dye on the relative dipole orientation are investigated. Chapter Three examines the dipole orientational control of simple four arm junctions (4AJs), which were immobilized on larger origami platforms. The cross-over location of this four-sequence DNA construct allows for close positioning of up to four individual dye molecules. The orientations of dyes in each of these four positions relative to their 4AJs are thus measured to investigate the site specific orientational dispersion. Finally, Chapter Four reviews the content of the previous two chapters and proposes possible directions for future research.

References

1 Theis, T. N. & Wong, H.-S. P. The end of moore's law: A new beginning for information technology. Computing in Science & Engineering 19, 41-50 (2017).

2 Steane, A. Quantum computing. Reports on Progress in Physics 61, 117-173, doi:10.1088/0034-4885/61/2/002 (1998).

3 Almudever, C. G. et al. in Design, Automation & Test in Europe Conference & Exhibition (DATE), 2017. 836-845.

4 O'Brien, J. L. Optical Quantum Computing. Science 318, 1567, doi:10.1126/science.1142892 (2007).

5 Yurke, B. & Kuang, W. Passive linear nanoscale optical and molecular electronics device synthesis from nanoparticles. Physical Review A 81, 033814, doi:10.1103/PhysRevA.81.033814 (2010).

6 Cannon, B. L. et al. Large Davydov Splitting and Strong Fluorescence Suppression: An Investigation of Exciton Delocalization in DNA-Templated Holliday Junction Dye Aggregates. The Journal of Physical Chemistry A 122, 2086-2095, doi:10.1021/acs.jpca.7b12668 (2018).

7 Engel, G. S. Quantum coherence in photosynthesis. Procedia Chemistry 3, 222-231 (2011).

8 Seeman, N. C. & Sleiman, H. F. DNA nanotechnology. Nature Reviews Materials 3, 17068 (2018).

9 Kasha, M., Rawls, H. R. & Ashraf El-Bayoumi, M. in Pure and Applied Chemistry Vol. 11 371 (1965).

10 Hübner, K. et al. Directing Single-Molecule Emission with DNA Origami-Assembled Optical Antennas. Nano Letters 19, 6629-6634, doi:10.1021/acs.nanolett.9b02886 (2019).

11 Rothemund, P. W. K. Folding DNA to create nanoscale shapes and patterns. Nature 440, 297-302 (2006).

12 Seeman, N. C. Nucleic acid junctions and lattices. Journal of theoretical biology 99, 237-247 (1982).

13 Seeman, N. C. Nanomaterials Based on DNA. Annual review of biochemistry 79, 65-87, doi:10.1146/annurev-biochem-060308-102244 (2010).

14 Zhang, F., Nangreave, J., Liu, Y. & Yan, H. Structural DNA Nanotechnology: State of the Art and Future Perspective. Journal of the American Chemical Society 136, 11198-11211, doi:10.1021/ja505101a (2014).

15 DeLuca, M., Shi, Z., Castro, C. E. & Arya, G. Dynamic DNA nanotechnology: toward functional nanoscale devices. Nanoscale Horizons 5, 182-201, doi:10.1039/C9NH00529C (2020).

16 Douglas, S. M. et al. Rapid prototyping of 3D DNA-origami shapes with caDNAno. Nucleic Acids Research 37, 5001-5006, doi:10.1093/nar/gkp436 (2009).

17 Castro, C. E. et al. A primer to scaffolded DNA origami. Nature Methods 8, 221-229, doi:10.1038/nmeth.1570 (2011).

18 Wang, P., Meyer, T. A., Pan, V., Dutta, P. K. & Ke, Y. The Beauty and Utility of DNA Origami. Chem 2, 359-382 (2017).

19 Klein, W. P. et al. Multiscaffold DNA Origami Nanoparticle Waveguides. Nano Letters 13, 3850-3856, doi:10.1021/nl401879r (2013).

20 Takabayashi, S. et al. High precision and high yield fabrication of dense nanoparticle arrays onto DNA origami at statistically independent binding sites. Nanoscale 6, 13928-13938, doi:10.1039/C4NR03069A (2014).

21 Bui, H. et al. Programmable Periodicity of Quantum Dot Arrays with DNA Origami Nanotubes. Nano Letters 10, 3367-3372, doi:10.1021/nl101079u (2010).

22 Yildiz, A. & Selvin, P. R. Fluorescence Imaging with One Nanometer Accuracy: Application to Molecular Motors. Accounts of Chemical Research 38, 574-582, doi:10.1021/ar040136s (2005).

23 Gordon, M. P., Ha, T. & Selvin, P. R. Single-molecule high-resolution imaging with photobleaching. Proceedings of the National Academy of Sciences of the United States of America 101, 6462, doi:10.1073/pnas.0401638101 (2004).

24 Rust, M. J., Bates, M. & Zhuang, X. Sub-diffraction-limit imaging by stochastic optical reconstruction microscopy (STORM). Nature Methods 3, 793-796, doi:10.1038/nmeth929 (2006).

25 Thompson, R. E., Larson, D. R. & Webb, W. W. Precise Nanometer Localization Analysis for Individual Fluorescent Probes. Biophysical Journal 82, 2775-2783, doi:https://doi.org/10.1016/S0006-3495(02)75618-X (2002).

26 Betzig, E. et al. Imaging Intracellular Fluorescent Proteins at Nanometer Resolution. Science 313, 1642, doi:10.1126/science.1127344 (2006).

27 Schnitzbauer, J., Strauss, M. T., Schlichthaerle, T., Schueder, F. & Jungmann, R. Super-resolution microscopy with DNA-PAINT. Nature protocols 12, 1198 (2017).

28 Jungmann, R. et al. Multiplexed 3D cellular super-resolution imaging with DNA-PAINT and Exchange-PAINT. Nature methods 11, 313 (2014).

29 Mortensen, K. I., Churchman, L. S., Spudich, J. A. & Flyvbjerg, H. Optimized localization analysis for single-molecule tracking and super-resolution microscopy. Nature methods 7, 377 (2010).

30 Dipole emission near planar interfaces in Principles of Nano-Optics (eds Bert Hecht & Lukas Novotny) 313-337 (Cambridge University Press, 2012).

31 Böhmer, M. & Enderlein, J. Orientation imaging of single molecules by wide-field epifluorescence microscopy. JOSA B 20, 554-559 (2003).

32 Bartko, A. P. & Dickson, R. M. Imaging three-dimensional single molecule orientations. The Journal of Physical Chemistry B 103, 11237-11241 (1999).

33 Lieb, M. A., Zavislan, J. M. & Novotny, L. Single-molecule orientations determined by direct emission pattern imaging. Journal of the Optical Society of America B 21, 1210-1215, doi:10.1364/JOSAB.21.001210 (2004).

34 Aguet, F., Geissbühler, S., Märki, I., Lasser, T. & Unser, M. Super-resolution orientation estimation and localization of fluorescent dipoles using 3-D steerable filters. Optics Express 17, 6829-6848, doi:10.1364/OE.17.006829 (2009).

35 Mortensen, K. I., Sung, J., Flyvbjerg, H. & Spudich, J. A. Optimized measurements of separations and angles between intra-molecular fluorescent markers. Nature communications 6, 8621 (2015).

CHAPTER TWO: QUANTIFICATION OF SINGLE MOLECULE ORIENTATION PRECISION USING DIPOLE IMAGING AND SUPER-RESOLUTION MICROSCOPY

This chapter was submitted to the American Chemical Society and is currently under review.

**This chapter contains modifications from the submitted text*

2.1 Quantification of Single Molecule Orientation Precision Using Dipole Imaging and Super-Resolution Microscopy

Brett Ward[1]

Christopher M. Green[1]

Wan Kuang[2]

Elton Graugnard[1]

[1]Micron School of Materials Science and Engineering, Boise State University

[2]Department of Electrical and Computer Engineering, Boise State University

Boise, Idaho USA 83725

2.2 Introduction

Control over the placement of molecules and nanoparticles enables novel materials and devices for applications ranging from energy harvesting to quantum computing[1,2]. Invented for the express purpose of positioning proteins, DNA nanotechnology has been employed to position fluorophores, proteins, and nanoparticles at the nanometer scale[3-6]. The popularity of DNA nanotechnology stems from the simplicity of Watson-Crick base paring for the design of nanostructures. While relative molecular orientations have been characterized with ensemble and single molecule measurements[7-17], the absolute precision with which DNA orients these molecules is not well understood. Here, we use dipole imaging and super-resolution microscopy to measure the precision with which DNA origami can orient single cyanine fluorophores. We find that the polar angle (θ) of the dye is controlled to within ~10° while the azimuthal angle (ϕ) varies considerably. These findings suggest that precise control of molecules using DNA origami may be more complicated than making simple chemical modifications to target component strands, and that there is still more to learn in order to understand the factors controlling structure in DNA-conjugated molecular systems.

The orientation of fluorophores in free space plays a critical role in energy transfer dynamics within molecular systems[18,19]. A fluorescent dye molecule, such as non-sulfonated cyanine 5 (diIC2(5)), behaves like a harmonic oscillator with dipole moment along the long axis of the molecule[12]. Determining the orientation of the oscillating dipole of fixed fluorophores has been of particular interest and is often achieved through absorption/emission polarization measurements and anisotropic point spread function (PSF) fitting[20-23]. When used in combination with total internal reflection fluorescence (TIRF) microscopy, molecular orientations in all three principle axes can be probed, which allows one to probe the local orientations of membranes or the alignments of DNA origami structures on a substrate[24,25]. Anisotropic PSF fitting of a single emitter takes advantage of the distinct emission pattern of a fixed fluorophore located near a dielectric interface to calculate the position of the dipole as well as the polar (θ) and azimuthal (ϕ) angles of the dipole[22,26-31].

In this work, we report measurements of the orientations of single dye molecules relative to the DNA double helices to which they are bound through the correlation of two single molecule (sm) optical techniques - defocused anisotropic PSF fitting and two-channel super-resolution microscopy with DNA points accumulation in nanoscale topography (DNA-PAINT)[26,32]. From these measurements, we determined the relative binding angles of internally bound dye molecules to the conjugated DNA and quantified the precision of dye molecule orientation control in a population of self-assembled DNA structures. To our knowledge, this work provides the first direct quantification of the precision with which DNA nanostructures can control the orientation of conjugated molecular systems.

2.3 Results

DNA origami cross-tile dimers[33,34] were adapted to serve as nanoscale imaging platforms for orientation measurements of single dye molecules (Figure 2.1a). Modifications to ssDNA staple strands at the ends of each of the six arms created docking sites for imager strand sequences (Section 2.8.1). By creating an asymmetric pattern, we were able to determine the in-plane orientation of the origami on the surface as well as confirm which face of the origami is in contact with the surface (Figures 2.13 and 2.14).

To position single molecules in predetermined locations within the DNA origami, a body staple on a single arm of one of the cross-tiles was modified internally with one of several conjugated dyes (Figure 2.1). Further, for the selected staple strand, the in-plane crossover locations within the cross-tile arm were used to infer the locations and orientations of each base in the double helix, as well as the positions of the dyes. The orientations of the embedded dyes were determined by imaging the single molecule dipole emission patterns, as discussed in the following sections.

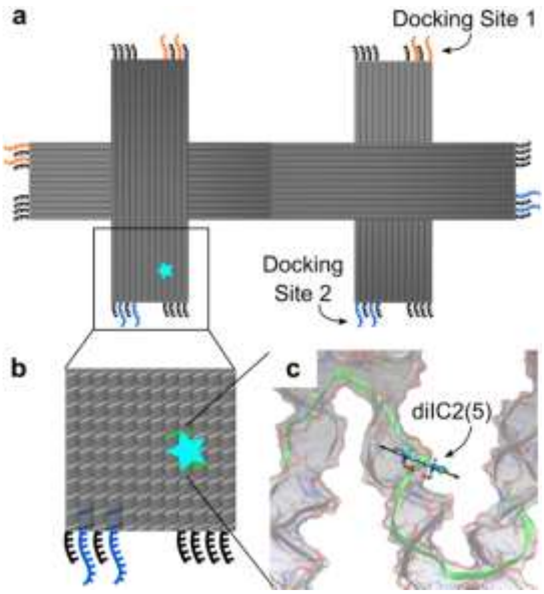

Figure 2.1 DNA origami nanoscale imaging platform for absolute orientation measurements in DNA-conjugated single molecule systems. (a) Two DNA origami cross-tiles, defined by their unique edge staples, are unified via sticky-end hybridization. The remaining arms contain docking sites (blue or orange) for transient hybridization of imager strands for Exchange-PAINT, as well as strands extended with poly-T to prevent blunt-end stacking (black strands). The asymmetric pattern of the docking sites allows for determination of face-up or face-down orientation as well as azimuthal orientation. Within one arm of the dimer, a single molecule (cyan star) is embedded via conjugation to a staple strand. (b) Enlarged view of the dimer arm indicated by the black square in (a), internal body staples are indicated by light gray ribbons. A single body staple (green ribbon) has been chemically modified with an internal dye modification to embed the dye in a specific position. (c) Atomic model depicting a possible orientation of a diIC2(5) phosphoramidite relative to the double-helix to which it is bound. The orientations of the bases in the helix are defined by the nearby crossovers of the staple, which are considered parallel to the global origami plane, creating a relatively consistent DNA structure. An arrow illustrates the dipole orientation of the fluorophore.

The DNA origami cross-tile dimer platforms measure ~100 nm long by ~200 nm wide (Figure 2.2a), and sub-diffraction imaging is required to optically resolve the features of individual structures. DNA-PAINT utilizes the transient binding between short dye-labelled ‘imager’ ssDNA strands with complementary ssDNA ‘docking sites’ extending from the arms of surface immobilized origami[32]. With sufficient integration time, the emission from these dynamic dyes can be modelled with a Gaussian distribution to find their centers with nanometer precision. To determine the orientations of origami cross-tile dimers on the surface, two imager solution washes (Exchange-PAINT) were performed for each experiment with each containing a unique imager strand sequence complementary to three specific arms of the origami dimers[35].

Using spherical gold nanoparticles bound to the surface as fiducial markers for image registration, the two SRM channels were correlated, as shown in Figure 2.2b. The composite two-color SRM image was then registered with the defocused sm-dipole emission pattern (Figure 2.2c), enabling correlation between single fluorescent molecules with their host origami platforms. In the three-color image of Figure 2.2d, the two-color SRM image is shown with the fitted sm-dipole emission pattern of a single diIC2(5) phosphoramidite embedded in the origami. For clarity, the emission pattern was scaled down from its defocused size.

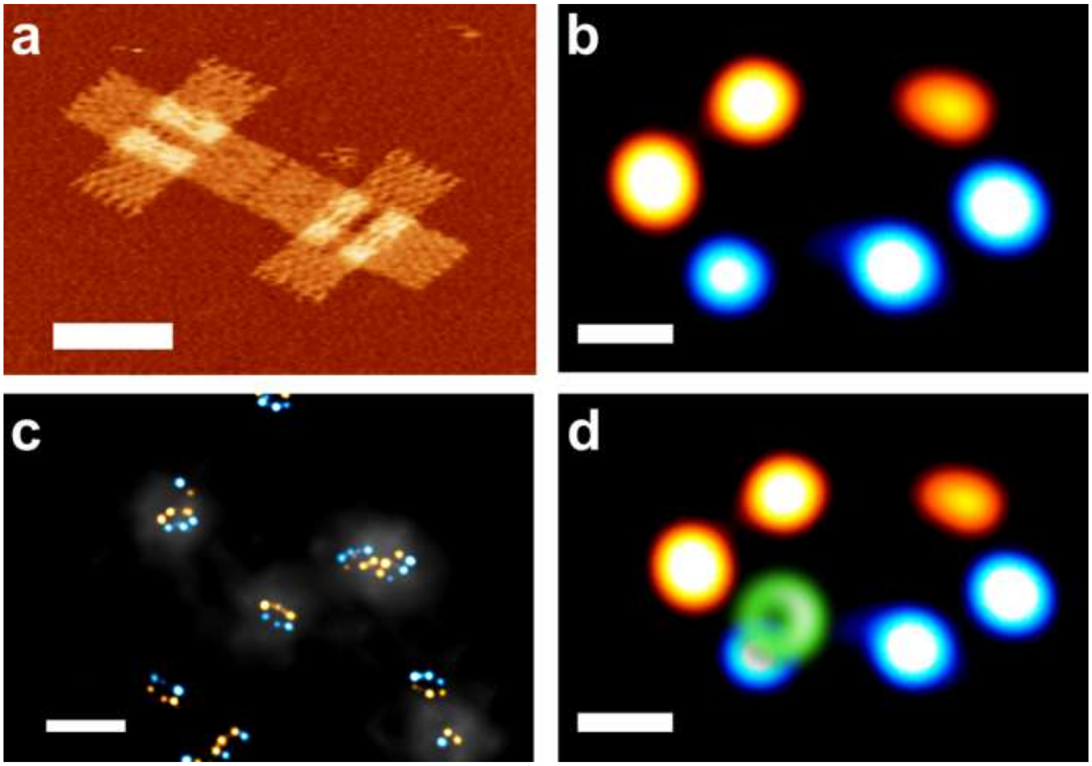

Figure 2.2: (a) Atomic force microscope (AFM) topographic image in fluid of a single origami cross-tile dimer showing the structure of the origami imaging platform. (b) Two-color super-resolution microscopy (SRM) image of a single DNA origami cross-tile dimer. The SRM channels are falsely colored to identify Docking Site 1 (orange) and Docking Site 2 (blue) tile arms. The asymmetry in the localization pattern allows us to determine that this dimer is face-up (Figure 2.13). (c) A three-channel composite image with sm-dipole emission patterns for diIC2(5) phosphoramidite embedded within the origami dimers. The white halos around the cross-tile dimers are the diIC2(5) emission from the defocused image. All three channels were aligned using AuNP fiducial markers in the full image (not shown). (d) The simulated emission pattern (green) from the observed sm-dipole signal overlaid on the origami dimer SRM pattern. Scale bars: 50 nm for a, b, and d, 500 nm for c.

When registered, the two-color SRM image and the fitted sm-dipole emission pattern share a common coordinate system, allowing calculation of the polar and azimuthal angles of the embedded dye relative to its helix in the DNA origami, as illustrated in Figure 2.3a. Consideration must be taken for the effects of electrostatic repulsion between neighboring DNA backbones, the effects of which cause a deflection of ~8° away from the principle axis of the helical domain, as observed experimentally in the weave pattern of the origami (Figure 2.2a), through coarse-grained modeling, and through atomistic molecular dynamics (Figure 2.17)[36]. The primary molecule studied in this work is the non-sulfonated phosphoramidite version of cyanine 5, diIC2(5), which is conjugated to the staple strand using two linkers (Figure 2.16)[37]. As discussed below, the single linker NHS ester of this dye was also investigated, as well as several other single-linker chromophores with similar emission spectra. An example of a three-channel sm-SRM image is shown in Figure 2.3b for a diIC2(5) phosphoramidite molecule embedded within an origami dimer. For this structure, the diIC2(5) was embedded midway between staple crossovers at “position 4” (Figure 2.6, Table 2.15) and was spatially accommodated within the staple by removing the thymine normally at that position of the sequence. The polar angle for the sm-dipole shown in Figure 2.3b was determined to be 26.5°, and its azimuthal angle relative to the origami coordinate system was 280° ± 10°, as indicated in the figure. Analysis of sm-dipole orientations for multiple origami dimers gave a structure-to-structure average polar angle of $\theta = 26° \pm 3°$, as illustrated in the upper schematic of Figure 2.3c. The azimuthal angles of the sm-dipoles relative to the origami coordinate system were less consistent between structures, with observed dipoles seemly three times as likely to adopt orientations perpendicular to the staple strand helical axis as adopting orientations parallel or transversal to the helix. This wide structure-to-structure variability of measured relative azimuthal angles is illustrated in the lower schematic of Figure 2.3c, which is a composite of the sm-dipole vector projections onto the plane of the origami (xy plane). In other words, while the embedded diIC2(5) phosphoramidite molecules exhibit a fairly consistent polar angle relative to the plane of the origami, there is large variability of the in-plane angle, relative to the helical axis, from one structure to another.

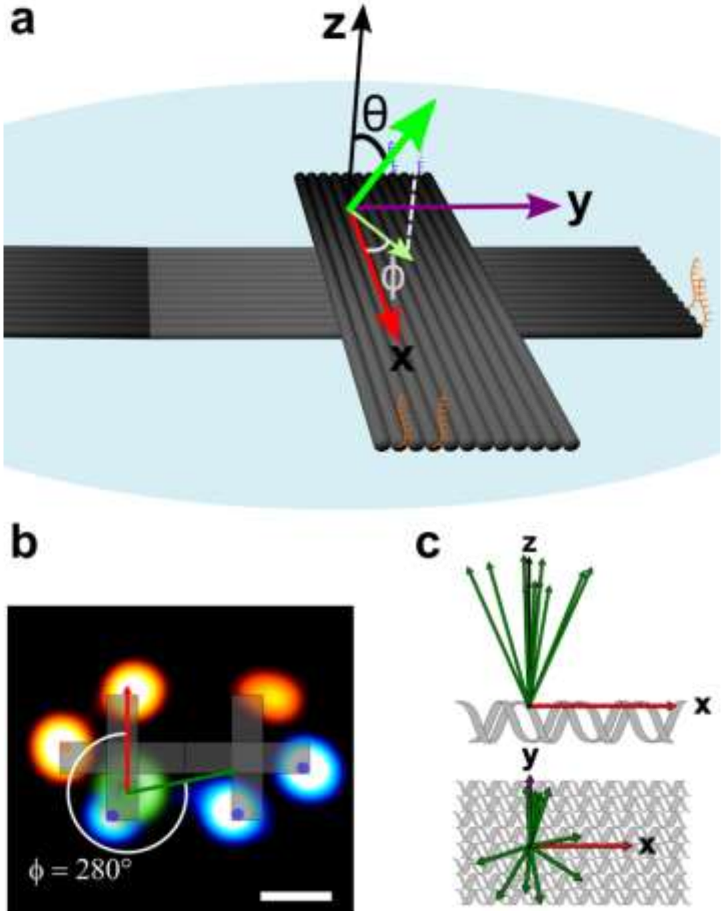

Figure 2.3: (a) Illustration of the coordinate system used to determine sm-dipole angles relative to the DNA imaging platform. Once the global orientation of the helical domain of the origami dimer is determined, it defines the x-axis (red arrow) on the DNA platform with positive x extending from the Docking Site 2 arm to the Docking Site 1 arm and the y (purple arrow) and z (black arrow) axes set using the right-hand rule. From sm-dipole analysis using MATLAB (Section 2.8.1.5), we calculated the polar and azimuthal angles (θ, ϕ) of the dipole relative to the local coordinate system. (b) An example of the SRM image of a DNA origami dimer with an emission pattern from an embedded diIC2(5) overlaid onto the three-channel image. The green arrow indicates the direction of the measured azimuthal angle of the observed dipole and a relative ϕ of 280° ± 10°. (c) Composite schematics of the observed polar angle (upper schematic, looking along the y-axis) and relative azimuthal angle (lower schematic, looking along the z-axis) for a single population of embedded diIC2(5) phosphoramidite molecules relative to the DNA structure (gray helices). Note, this composite shows static diIC2(5) emission dipole orientations from ten separate DNA origami structures; this composite does not indicate temporal fluctuations of a single embedded molecule. Scale bar: 50 nm.

For the system shown in Figure 2.3, the staple strand that was used to embed the diIC2(5) was modified by removing a thymine at the diIC2(5) position to accommodate for the dye. Thus, the diIC2(5) phosphoramidite was accommodated into the sequence by replacing a base in the staple strand and, when folded into the DNA origami, the diIC2(5) was opposite an unpaired adenine base. To further constrain the diIC2(5) in the origami, a staple strand that was fully complementary to the scaffold domain was modified with the dye. The diIC2(5) phosphoramidite was positioned at the same point in the sequence (position 4 in Figure 2.6; all dye modified staple strand sequences are listed in Tables 2.15, 2.16). sm-SRM results indicate that the unaccommodated diIC2(5) has a similar polar angle and dispersion, $\theta = 26° \pm 4°$, and again a slight majority of measured relative ϕ found within 20° of perpendicular to the helical axis. However, when viewed as an entire dataset, the azimuthal angles observed for multiple origami dimers are fairly dispersed about the helical axis.

2.3.1 Sequence Location Dependence of Dipole Angles

We assume the local base pair pitch and orientation is consistent among the population of origami. Thus, we expected that moving the location of the internal diIC2(5) phosphoramidite in the sequence would create a measurable difference in the orientation of the dipole relative to the dsDNA staple strand. As summarized in Figure 2.4, six versions of the unaccommodated diIC2(5) phosphoramidite were analyzed independently. For these versions, the position of the internal diIC2(5) was sequentially shifted by two bases with a total of ten bases between the extreme locations of the dye. The locations of the dye are illustrated in Figure 2.6 and modeled in Figure 2.17. Figure 2.4a plots the average polar angle and standard deviation for each position of the internal diIC2(5) within the staple strand. These data are enumerated in Figure 2.4b, which also plots projections of the sm-dipoles into the xy-plane for each dye position. As expected for these positions along the helix, there was a clear trend in the polar angle; however, in all cases, the azimuthal angle is scattered among the measured structures at each dye position.

2.3.2 NHS Ester Single-Linker Dipole Orientations

In addition to the embedded two-tether diIC2(5) phosphoramidite dye configurations, the relative orientations of five single-tether NHS ester dyes were examined. Dyes with similar excitation and emission spectra to the diIC2(5) phosphoramidite were chosen, namely diIC2(5)N, SeTau 647N, DyLight 650N, ATTO 647N, and Alexa 647N. These dyes were located at position 4 of the staple strand (position 5 for diIC2(5)N due to synthesis restrictions; sequences provided in Table 2.16). The single-tether diIC2(5)N measured the largest polar angle, $\theta = 35° \pm 4°$, while the rest of the NHS ester dyes had polar angles more consistent with the two-tether diIC2(5) immobilized at position 4, as seen in Figure 2.4a, circles. The lowest row of Figure 2.4c shows a similarly large structure-to-structure dispersion of azimuthal angles for each of the NHS ester dyes. Here, dispersion in structure-to-structure orientation could result from temporal variations in single-tether dyes, which can be expected to fluctuate considerably, yet the standard deviation of the polar angles was surprisingly low, which may indicate that the dyes are locally fixed within metastable configurations.

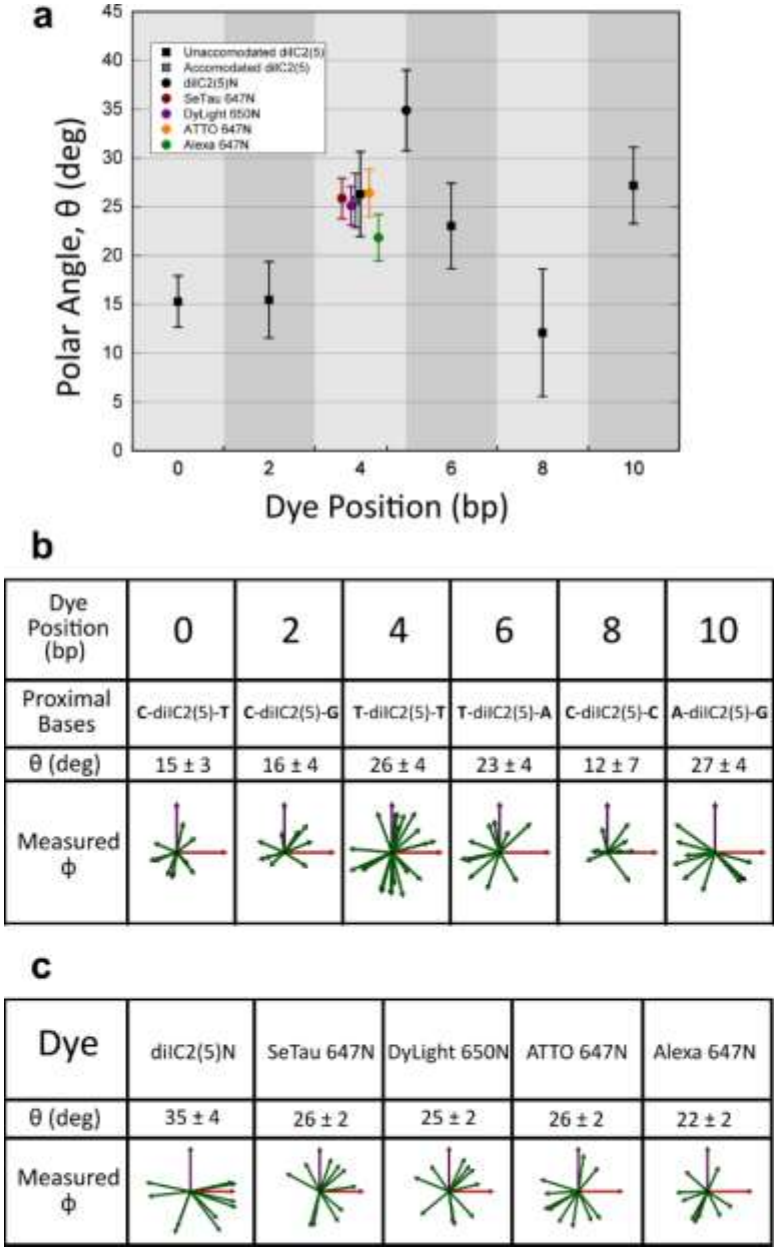

Dye Position (bp)	0	2	4	6	8	10
Proximal Bases	C-diIC2(5)-T	C-diIC2(5)-G	T-diIC2(5)-T	T-diIC2(5)-A	C-diIC2(5)-C	A-diIC2(5)-G
θ (deg)	15 ± 3	16 ± 4	26 ± 4	23 ± 4	12 ± 7	27 ± 4
Measured φ						

Dye	diIC2(5)N	SeTau 647N	DyLight 650N	ATTO 647N	Alexa 647N
θ (deg)	35 ± 4	26 ± 2	25 ± 2	26 ± 2	22 ± 2
Measured φ					

Figure 2.4: (a) The average measured polar angle and standard error for all dyes studied. The data for each population of unaccommodated diIC2(5) phosphoramidite, at different positions along the double helix, are shown as black squares. The 10 base pair separation between the two extreme positions constitutes a full turn of the B-DNA helix. The data for several other dyes at position 4 include the accommodated diIC2(5) phosphoramidite (black square with cross hatch), diIC2(5)N (black circle), SeTau 647N (maroon circle), DyLight 650N (purple circle), ATTO 647N (orange circle), and Alexa 647N (green circle). (b) The dye position in base pairs, the proximal bases about each diIC2(5), and the observed polar angle values and the relative azimuthal angle dispersions at each position for the unaccommodated diIC2(5) phosphoramidite. (c) Observed polar angle values and the relative azimuthal angle dispersions of the single-linker NHS ester dyes at position 4.

2.4 Discussion

Molecules bound to dsDNA with two tethers, such as the diIC2(5) studied here, are expected to have stable orientations over the time scales in which they were measured[15]. This implies that the structure-to-structure dispersion observed in sm-dipole orientations relative to their staple strand is a result of variations in the local environment of each origami structure. Cryo-EM imaging of DNA origami with near atomic resolution has previously provided strong evidence for high ordering across a population of structures[38]. However, self-assembly of DNA origami is not a perfect process and some percentage of folding errors will be present in a given population[39]. Even within ideal structures, origami structure formation follows complex folding pathways, which may contribute to the orientational variations observed[40]. Our results suggest these minute discrepancies have a major effect on individual structures when directly measuring single molecule orientations. The highest structural resolution of DNA nanostructures has been achieved for non-scaffolded systems, such as the tensegrity triangle, but even small sequence variations have major impacts on the crystal structure resolution. Further, when cyanine phosphoramidites were inserted into tensegrity triangles, the dyes could not be atomically resolved despite a 5 Å crystal resolution[41,42].

It is worth noting that of the 93% of the DNA origami cross-tile dimers observed in this study were found in the face-down configuration, possibly due to the high curvature of the origami creating a more favorable DNA-glass interaction surface in this landing orientation. When the origami is face-down, dyes located at position 4 are proximal to the glass surface and positions 0, 8 and 10 are away from the glass, as well as positions 2 and 6 to a lesser degree. If short-range dye/glass interactions were the source of disparity in observed dipole orientations relative to their DNA substrates, we would expect the distribution of dipole orientations at position 4 to differ noticeably from the other positions. However, the dispersion in both polar and azimuthal angles is similar for all locations, as seen in Figure 2.4. Another perspective is provided by Figure 2.15, which shows a plot of the azimuthal angle as a function of polar angle for all observed structures highlighting both the relative consistency in the polar angle and large variations in azimuthal angle for all positions. If long-range factors influence the dyes, such as non-uniformities of the electric double layer formed at the glass surface, then the dye orientation dispersion may indicate that surface heterogeneity cannot be neglected. The DNA and tethers may not be sufficient to maintain a dye's orientation in the presence of potential variations from trapped surface charge or fluctuations in local ionic strength.

Within the DNA nanostructures, another possible explanation for the seemingly random nature of dipole orientations at each position is a sufficiently flat energy landscape at each position. The lack of a deep energy well to constrain the dipoles to a well-defined orientation and the relatively open structure of the origami compared to the dimensions of the dyes (see Figure 2.17) allows the dyes sufficient freedom to achieve any of a number of configurations. This interpretation is supported by energy surface modeling for a conjugated diIC2(3) system, which found a textured but large energy well for non-intercalated dyes[43]. In our own computational modelling of a diIC2(5) phosphoramidite molecule embedded within an origami, we observed temporal variations in the polar angles that agree well with our experimental data (Figure 2.18). However, on the few nanosecond time-scale of the simulations (2.8.1.6 Computational Modeling), the temporal variations of the azimuthal angles were significantly smaller than the structure-to-structure variation in experimental azimuthal angles. The agreement in polar angle variation is promising and may indicate a lower bound to dye orientation precision, but additional work, such as including the effect of a surface or non-ideal origami foldings, are needed to establish the source of the dispersion in azimuthal angles.

Relative to applications of DNA-conjugated chromophore systems, our results suggest that ensemble measurements of monomer populations may exhibit a large degree of inhomogeneous spectral broadening if these orientation variations lead to spectral variations. Certainly, aggregates of multiple dyes may be expected to exhibit considerable variation in coupling unless the aggregate interactions lead to preferential relative orientations through weak bonding, but this would be possible only in the most closely assembled aggregates[7,44]. FRET systems must be examined more closely since these orientation variations can be expected to create dispersion in the FRET efficiency, as has been observed[45]. Thus, the measurements reported here provide insight into the origins of this dispersion. The complexities of DNA origami could be avoided by conjugating dyes to simpler duplex constructs which may result in lower orientation variations, as observed for terminally conjugated CyX systems[10,11]. Immobilization of such systems using the approach reported here is a promising approach for further quantifying the precision with which DNA can control the position and orientation of molecular components.

2.5 Conclusions

The orientations of fluorescent molecules internally embedded in DNA origami relative to the local helical axis of the dsDNA have been quantified for several different dye and structure configurations. DNA origami has the ability to position the polar angle of an internal dye with reasonable precision within a population of structures. The precision of the azimuthal angle within all studied structures suggests that DNA origami may require additional modifications to enable molecular positioning when absolute angular precision is a necessity, such as when attempting to assemble complex photonic and excitonic devices.

Ionic strength dependent hydrostatic repulsion of the sugar-phosphate backbones within DNA origami create a weave pattern that makes determining the absolute orientation of the immediate dsDNA environment around the dye molecule difficult. Further work is needed to understand how the relative binding angles of internal dyes within dsDNA are affected by environmental influences such as proximal bases about the dye, buffer salt type and concentration, and folding conditions within a population of structures. The work described above outlines a single instrument method for measuring dye molecule orientations and orientation of the dsDNA substrate to which they are bound and provides insight into the precision of dye positioning within a population of self-assembled DNA origami. Application of this technology to other DNA-based molecular positioning systems will yield valuable insights into the precision of molecular control that can be achieved.

2.6 Acknowledgments

We thank members of the Nanoscale Materials and Device group at Boise State University for valuable assistance and discussions. The optical microscope used in this work was paid for by DARPA Contract No. N66001-08-1-2018. Select oligos, optical components, and chemicals used in this work were paid for by Grant No. 1648655 from the National Science Foundation. The computing cluster used for NAMD modeling was supported by the National Science Foundation under Grant No. 1229709.

2.7 References

1 Langlais, M., Hugonin, J.-P., Besbes, M. & Ben-Abdallah, P. Cooperative electromagnetic interactions between nanoparticles for solar energy harvesting. *Optics express* **22**, A577-A588 (2014).

2 Yurke, B. & Kuang, W. Passive linear nanoscale optical and molecular electronics device synthesis from nanoparticles. *Physical Review A* **81**, 033814, doi:10.1103/PhysRevA.81.033814 (2010).

3 Takabayashi, S. *et al.* High precision and high yield fabrication of dense nanoparticle arrays onto DNA origami at statistically independent binding sites. *Nanoscale* **6**, 13928-13938, doi:10.1039/C4NR03069A (2014).

4 Schreiber, R. *et al.* Hierarchical assembly of metal nanoparticles, quantum dots and organic dyes using DNA origami scaffolds. *Nature Nanotechnology* **9**, 74, doi:10.1038/nnano.2013.253 (2013).

5 Seeman, N. C. & Sleiman, H. F. DNA nanotechnology. *Nature Reviews Materials* **3**, 17068 (2018).

6 Seeman, N. C. Nucleic acid junctions and lattices. *Journal of theoretical biology* **99**, 237-247 (1982).

7 Cannon, B. L. *et al.* Coherent Exciton Delocalization in a Two-State DNA-Templated Dye Aggregate System. *The Journal of Physical Chemistry A* **121**, 6905-6916, doi:10.1021/acs.jpca.7b04344 (2017).

8 Heussman, D. *et al.* Measuring local conformations and conformational disorder of (Cy3) 2 dimer labeled DNA fork junctions using absorbance, circular dichroism and two-dimensional fluorescence spectroscopy. *Faraday Discussions* (2019).

9 Kringle, L. *et al.* Temperature-dependent conformations of exciton-coupled Cy3 dimers in double-stranded DNA. *The Journal of chemical physics* **148**, 085101 (2018).

10 Ouellet, J., Schorr, S., Iqbal, A., Wilson, Timothy J. & Lilley, David M. J. Orientation of Cyanine Fluorophores Terminally Attached to DNA via Long, Flexible Tethers. *Biophysical Journal* **101**, 1148-1154, doi:10.1016/j.bpj.2011.07.007 (2011).

11 Iqbal, A. *et al.* Orientation dependence in fluorescent energy transfer between Cy3 and Cy5 terminally attached to double-stranded nucleic acids. *Proceedings of the National Academy of Sciences* **105**, 11176, doi:10.1073/pnas.0801707105 (2008).

12 Ranjit, S., Gurunathan, K. & Levitus, M. Photophysics of Backbone Fluorescent DNA Modifications: Reducing Uncertainties in FRET. *The Journal of Physical Chemistry B* **113**, 7861-7866, doi:10.1021/jp810842u (2009).

13 Moerner, W. E. & Fromm, D. P. Methods of single-molecule fluorescence spectroscopy and microscopy. *Review of Scientific Instruments* **74**, 3597-3619, doi:10.1063/1.1589587 (2003).

14 Tamarat, P., Maali, A., Lounis, B. & Orrit, M. Ten years of single-molecule spectroscopy. *The Journal of Physical Chemistry A* **104**, 1-16 (2000).

15 Mortensen, K. I., Sung, J., Flyvbjerg, H. & Spudich, J. A. Optimized measurements of separations and angles between intra-molecular fluorescent markers. *Nature communications* **6**, 8621 (2015).

16 Backer, A. S., Lee, M. Y. & Moerner, W. E. Enhanced DNA imaging using super-resolution microscopy and simultaneous single-molecule orientation measurements. *Optica* **3**, 659-666, doi:10.1364/OPTICA.3.000659 (2016).

17 Backer, A. S. *et al.* Single-molecule polarization microscopy of DNA intercalators sheds light on the structure of S-DNA. *Science Advances* **5**, eaav1083, doi:10.1126/sciadv.aav1083 (2019).

18 Kasha, M., Rawls, H. R. & Ashraf El-Bayoumi, M. in *Pure and Applied Chemistry* Vol. 11 371 (1965).

19 Dale, R. E., Eisinger, J. & Blumberg, W. The orientational freedom of molecular probes. The orientation factor in intramolecular energy transfer. *Biophysical journal* **26**, 161-193 (1979).

20 Bartko, A. P. & Dickson, R. M. Imaging three-dimensional single molecule orientations. *The Journal of Physical Chemistry B* **103**, 11237-11241 (1999).

21 Ha, T., Laurence, T. A., Chemla, D. S. & Weiss, S. Polarization Spectroscopy of Single Fluorescent Molecules. *The Journal of Physical Chemistry B* **103**, 6839-6850, doi:10.1021/jp990948j (1999).

22 Lieb, M. A., Zavislan, J. M. & Novotny, L. Single-molecule orientations determined by direct emission pattern imaging. *Journal of the Optical Society of America B* **21**, 1210-1215, doi:10.1364/JOSAB.21.001210 (2004).

23 Lethiec, C. *et al.* Measurement of three-dimensional dipole orientation of a single fluorescent nanoemitter by emission polarization analysis. *Physical Review X* **4**, 021037 (2014).

24 Sund, S. E., Swanson, J. A. & Axelrod, D. Cell Membrane Orientation Visualized by Polarized Total Internal Reflection Fluorescence. *Biophysical Journal* **77**, 2266-2283, doi:10.1016/S0006-3495(99)77066-9 (1999).

25 Gopinath, A. *et al.* Absolute and arbitrary orientation of single molecule shapes. *arXiv preprint arXiv:1808.04544* (2018).

26 Aguet, F., Geissbühler, S., Märki, I., Lasser, T. & Unser, M. Super-resolution orientation estimation and localization of fluorescent dipoles using 3-D steerable filters. *Optics Express* **17**, 6829-6848, doi:10.1364/OE.17.006829 (2009).

27 Mortensen, K. I., Churchman, L. S., Spudich, J. A. & Flyvbjerg, H. Optimized localization analysis for single-molecule tracking and super-resolution microscopy. *Nature methods* **7**, 377 (2010).

28 Patra, D., Gregor, I. & Enderlein, J. Image Analysis of Defocused Single-Molecule Images for Three-Dimensional Molecule Orientation Studies. *The Journal of Physical Chemistry A* **108**, 6836-6841, doi:10.1021/jp048188m (2004).

29 Hellen, E. H. & Axelrod, D. Fluorescence emission at dielectric and metal-film interfaces. *JOSA B* **4**, 337-350 (1987).

30 Bartko, A. P. & Dickson, R. M. Three-dimensional orientations of polymer-bound single molecules. *The Journal of Physical Chemistry B* **103**, 3053-3056 (1999).

31 Böhmer, M. & Enderlein, J. Orientation imaging of single molecules by wide-field epifluorescence microscopy. *JOSA B* **20**, 554-559 (2003).

32 Schnitzbauer, J., Strauss, M. T., Schlichthaerle, T., Schueder, F. & Jungmann, R. Super-resolution microscopy with DNA-PAINT. *Nature protocols* **12**, 1198 (2017).

33 Liu, W., Zhong, H., Wang, R. & Seeman, N. C. Crystalline Two-Dimensional DNA-Origami Arrays. *Angewandte Chemie International Edition* **50**, 264-267, doi:10.1002/anie.201005911 (2011).

34 Green, C. M. *et al.* Metrology of DNA arrays by super-resolution microscopy. *Nanoscale* **9**, 10205-10211, doi:10.1039/C7NR00928C (2017).

35 Jungmann, R. *et al.* Multiplexed 3D cellular super-resolution imaging with DNA-PAINT and Exchange-PAINT. *Nature methods* **11**, 313 (2014).

36 Snodin, B. E., Schreck, J. S., Romano, F., Louis, A. A. & Doye, J. P. Coarse-grained modelling of the structural properties of DNA origami. *Nucleic acids research* **47**, 1585-1597 (2019).

37 Kumari, N., Ciuba, M. A. & Levitus, M. Photophysical properties of the hemicyanine Dy-630 and its potential as a single-molecule fluorescent probe for biophysical applications. *Methods and applications in fluorescence* **8**, 015004 (2019).

38 Bai, X.-c., Martin, T. G., Scheres, S. H. W. & Dietz, H. Cryo-EM structure of a 3D DNA-origami object. *Proceedings of the National Academy of Sciences* **109**, 20012, doi:10.1073/pnas.1215713109 (2012).

39 Wagenbauer, K. F., Wachauf, C. H. & Dietz, H. Quantifying quality in DNA self-assembly. *Nature Communications* **5**, 3691, doi:10.1038/ncomms4691 (2014).

40 Lee Tin Wah, J., David, C., Rudiuk, S., Baigl, D. & Estevez-Torres, A. Observing and Controlling the Folding Pathway of DNA Origami at the Nanoscale. *ACS Nano* **10**, 1978-1987, doi:10.1021/acsnano.5b05972 (2016).

41 Zheng, J. *et al.* From molecular to macroscopic via the rational design of a self-assembled 3D DNA crystal. *Nature* **461**, 74-77 (2009).

42 Wang, T. *et al.* A DNA crystal designed to contain two molecules per asymmetric unit. *Journal of the American Chemical Society* **132**, 15471-15473 (2010).

43 Stennett, E. M., Ma, N., Van Der Vaart, A. & Levitus, M. Photophysical and dynamical properties of doubly linked Cy3–DNA constructs. *The Journal of Physical Chemistry B* **118**, 152-163 (2014).

44 Cannon, B. L. et al. Large Davydov Splitting and Strong Fluorescence Suppression: An Investigation of Exciton Delocalization in DNA-Templated Holliday Junction Dye Aggregates. The Journal of Physical Chemistry A 122, 2086-2095, doi:10.1021/acs.jpca.7b12668 (2018).

45 Stein, I. H., Steinhauer, C. & Tinnefeld, P. Single-Molecule Four-Color FRET Visualizes Energy-Transfer Paths on DNA Origami. *Journal of the American Chemical Society* **133**, 4193-4195, doi:10.1021/ja1105464 (2011)

2.8 Supplementary Information

2.8.1 Methods

2.8.1.1 DNA Origami Synthesis and Dimerization

The component A and B DNA origami cross-tiles where folded separately by annealing a solution of 1:5:10 scaffold strands (Bayou BioLabs) to body staples to edge staples (Integrated DNA Technologies) in a 0.5X TBE buffer containing 12.5 mM $MgCl_2$[1,2]. The body staple with an internal dye modification (CO-M-106-X, Figure 2.6 and Tables 2.15 and 2.16) was substituted for CO-M-106 in the A-tile only and at a 10:1 staple to scaffold ratio. Non-labeled oligos and scaffold strand were purchased with standard desalting and used as received. Dye-labeled oligos, all purchased from Integrated DNA Technologies, were purified with HPLC and used without further purification. Annealed solutions where purified via gel electrophoresis in a 0.8% agarose gel prepared with 0.5X TBE, 8 mM $MgCl_2$. DNA origami dimers where formed by mixing equal concentrations of A-tiles and B-tiles in a 0.5X TBE buffer with 15 mM $MgCl_2$ and incubated at ambient temperature for at least 24 hours before imaging. A small volume (5 µL) of each sample solution was imaged using atomic force microscopy (AFM, Figure 2.5) to insure proper dimer formation before fluorescence imaging. All solutions were stored in a dark environment when not being measured.

2.8.1.2 Sample Preparation

Glass coverslips were functionalized on one side with 150 nm silane gold nanoparticles (NanoPartz) to act as fiducial markers to correct for stage drift while imaging and to allow for image registration across multiple channels[3]. The glass cover slip was prepared for DNA-PAINT super-resolution microscopy using a method to be published and then assembled into a custom, reusable, open-well microscope slide. DNA origami dimers were deposited at a low concentration (5 pM) to be directly adsorbed onto the glass surface amongst the dispersed gold nanoparticles. Each sample was incubated at ambient temperature for 10 minutes before imaging. DNA-PAINT imaging of cross-tile origami on glass cover slips was found to be incompatible with the common PCA/PCD oxygen scavenger, and so no triplet state quenching or oxygen scavenging system was employed during this study.

2.8.1.3 Dipole Imaging

For single molecule (sm) dipole imaging, the fluorescence of single embedded dye molecules was measured on a custom microscope (Figure 2.7) built around a Nikon Ti-U inverted microscope with a Nikon CFI Apochromat TIRF 100x oil immersion objective (NA = 1.49). Defocus was achieved by bringing the gold nanoparticles on the surface into sharp focus using room light and then stepping the z-piezo stage (Mad City Labs Inc.) 200-600 nm toward the objective. Embedded dyes were excited with a 640 nm laser diode (QLD-640-100S, QPhotonics) coupled into the fiber port of a Nikon TIRF Illuminator (TI-TIRF-E) mounted to the lower filter turret via a 561 nm/640 nm fiber combiner (Custom RG45A1, ThorLabs) and the angle of incidence of the excitation beam was adjusted until the S/N was optimized. A λ/2 wave plate was placed in the beam path to control the non-uniform polarization of the laser diode prior to imaging. A quad band excitation filter (ZET405/488/561/640xv2, Chroma) and beam splitter (ZT405/488/561/640rpcv2, Chroma) was used to clean up the excitation source and a quad band emission filter (ZET405/488/561/640m-TRFv2, Chroma) isolated the emission from single diIC2(5) molecules, which was then collected by a Princeton

Instruments ProEM: 512B+ EMCCD with an EM gain of 100X. A diagram of the microscope setup for dipole imaging can be seen in Figure 2.7a. The integration time for each captured frame was 250 ms. A representative image of dipole emission from diIC2(5) phosphoramidite immobilized in DNA origami is shown in Figure 2.8.

2.8.1.4 Super-Resolution Imaging

Immediately following single molecule dipole imaging, the optical system was reconfigured to image Cy3b fluorophores for Exchange-PAINT super-resolution microscopy (SRM) of the same area[4]. For SRM, the excitation source was a 561 CW laser (Coherent Sapphire FP) coupled through the same fiber combiner as above and the beam angle was readjusted to optimize S/N. The optical path remained nearly the same as above with the addition of a 650 nm SP dichroic mirror placed in the optical path in the upper filter turret to allow for a custom focal drift correction system to operate during the extended SRM imaging times. A diagram of the microscope setup for SRM can be seen in Figure 2.7b, and sequences of the imager strands are given in Table 2.17. The imaging buffer was exchanged with a 0.5X TBE solution with 35 mM $MgCl_2$ and 3 nM Imager Strand 1. Post data collection of Docking Sites 1, a solution of ssDNA complementary with Imager Strand 1 was added at 1000:1 excess to quench the blinking at Docking Sites 1. A buffer exchange was then performed with 3 nM Imager Strand 2, 35 mM $MgCl_2$ to resolve Docking Sites 2. All SRM was performed at 150 ms/frame for 10,000 frames with an EM gain of 50X. Figures 2.9 and 2.10 show representative SRM images of Docking Sites 1 and 2, respectively, for the same area of the sample. Combining these images yields the composite two-color SRM image shown in Figure 2.11, which allows determination of the DNA origami dimer orientations.

2.8.1.5 Image Processing

Individual frames of defocused sm-dipole PSFs were analyzed using the steerableDipoleDetector MATLAB algorithm to extract the polar (θ) and azimuthal (ϕ) dipole angles[5]. SRM image stacks were analyzed using the THUNDERSTORM ImageJ plug-in[6]. The resulting detected sm-dipole and SRM localization outputs were thresholded individually to remove background signals. Using the AuNPs as registration marks, images from the three channels were overlaid to create a master image in ImageJ, as shown in Figure 2.12. From the master image, sm-dipole orientations, which can be confirmed to originate from a specific DNA origami dimer, are compared to the DNA helical axis orientation at the embedded dye location to extract sm-dipole orientations relative to their dsDNA substrate as shown in Figure 2.3b. The number of structures analyzed, *n*, for structures with diIC2(5) molecules at an unaccommodated position 4 is 21 (shown in Figure 2.19) and for position 8 is 11. For all other structures studied, $n = 10$.

2.8.1.6 Computational Modeling

Computational modeling was performed on a 32-node CPU/GPU computing cluster (http://coen.boisestate.edu/hpc/) using the NAMD software package, and the protocol for modeling of DNA origami was implemented with a magnesium hexahydrate ($MgHH^{2+}$) concentration of ~12.5 mM[7,8]. Modeling results were visualized using VMD, including the use of msms. For the simulations, a pseudo-section of the DNA origami cross-tile arm near the CO-M-106 staple strand was generated using cadnano2 and uploaded to the ENRG MD server to generate the necessary NAMD input files (http://bionano.physics.illinois.edu/origami-structure)[9]. A model of the diIC2(5) was generated using Avogadro ver. 1.2 (Figure 2.16) (http://avogadro.cc) and further refined using the Molefacture extension for VMD[10]. CHARMM parameters for the diIC2(5) phosphoramidite were derived from those reported for non-sulfonated Cy3, diIC2(3)[11]. VMD was used to insert the diIC2(5) into the backbone of the CO-M-106 staple strand at each position studied experimentally. To determine the computed angles of the diIC2(5), the coordinates of the nitrogen atoms were used to define the molecule's dipole moment vector. The polar (θ) and azimuthal (ϕ) angels were then calculated for each trajectory frame of the final unconstrained simulation at 2 fs steps for 4.8 ns.

2.8.2 Data Analysis

2.8.2.1 Defining the Origami Substrate Coordinate System

DNA origami cross-tile dimers contain three separate helical domains as shown in Figure 2.13a. The first domain extends across the length of the dimer and is defines the major axis. Two additional domains are oriented perpendicular to the major axis and are unique to the origami monomer to which they belong, minor axis A and minor axis B. As shown in Figures 2.13b and c, a DNA origami cross-tile dimer may land on the surface in either a "face-up" or "face-down" orientation. The asymmetrical patterns of Docking Site 1 and Docking Site 2 in SRM images make determining the landing orientation possible. The face-up and face-down orientations are defined as shown in 2.13b. The helical domain that serves as the dsDNA substrate for embedding the dye molecules is located on minor axis A, shown as a green star in Figure 2.13a and b. Determining the global angle of the minor axis A helical domain for any individual structure is accomplished in the following manner (illustrated in Figure 2.13c): Using ImageJ image processing and analysis software, the global angle of the line between the two SRM locations on the major axis from Docking Site 1 to Docking Site 2 is measured relative to the image. The uncertainty in the SRM localizations propagates into uncertainty in the angle measurement, the extreme angles from the edges of the localizations are used to calculate the error in the helical domain angle (dotted yellow arrows). Because the two SRM sites are not located on the same helix along the major axis, the global angle of the minor axis A is not perpendicular to this angle but is instead the obtuse angle is calculated to be 100° assuming a helix diameter of 2 nm. Additionally, coarse-grain modelling has shown a local helix deflection of 8° due to hydrostatic repulsion of the sugar-phosphate backbones within DNA origami[12]. Local deflection is CCW when the dimer is face-up and CW when face-down. Thus, the value of 108° was used to calculate the helical domain angle at the embedded dye location from the measured major axis angle according to the landing orientation of each origami. This calculated angle was confirmed through both AFM and SRM images.

2.8.2.2 Standardizing Dipole Orientation Relative to the dsDNA Substrate.

To avoid creating artifacts in the data, all relative azimuthal (ϕ) angles are reported as what would be measured from face-up DNA origami dimers. That is, when a dimer was observed to be face-down, 180° was subtracted from the calculated relative azimuthal angle to normalize the observed diffraction pattern to a standard global coordinate system as shown in Figure 2.14. This step is necessary due to the limits of optical system which can only record the portion of the emission field collected by the objective. The measured value of theta is restricted to between 0 and +90° by the fitting algorithm. We assume the polar (θ) angle is symmetrical about the surface plane and therefore is not affected by the normalization.

2.8.2.3 Structure Selection for Orientation Measurements of Embedded Dyes in dsDNA

For each structure, three-channel master images of DNA origami cross-tiles on a glass surface were constructed by superimposing 40x magnification super-resolution (SRM) images of Docking Site 1 and Docking Site 2 onto appropriately scaled defocused sm-dipole images using immobilized gold nanoparticles (AuNPs) as registration marks. Even though the scattering signal of 150 nm AuNPs in the dipole channel is low, proper registration can be achieved with some effort. Non-overlapping sm-dipole emission patterns with origami cross-tile dimer SRM patterns present in the center of the pattern were identified for further analysis. Within this subset of data, if multiple cross-tile dimers, cross-tile monomers, or aggregations of DNA were observed in the SRM channels in the near vicinity of the sm-dipole pattern, the structure was thrown out. Additionally, structures were discarded when the cross-tile in the center of the emission pattern lacked sufficient structural information in the SRM channels to determine the orientation of the helical domain of the dsDNA substrate. Only structures with sm-dipole emission patterns corresponding to a distinct origami cross-tile dimers with measurable orientations were analyzed further.

2.8.3 Supplementary Figures

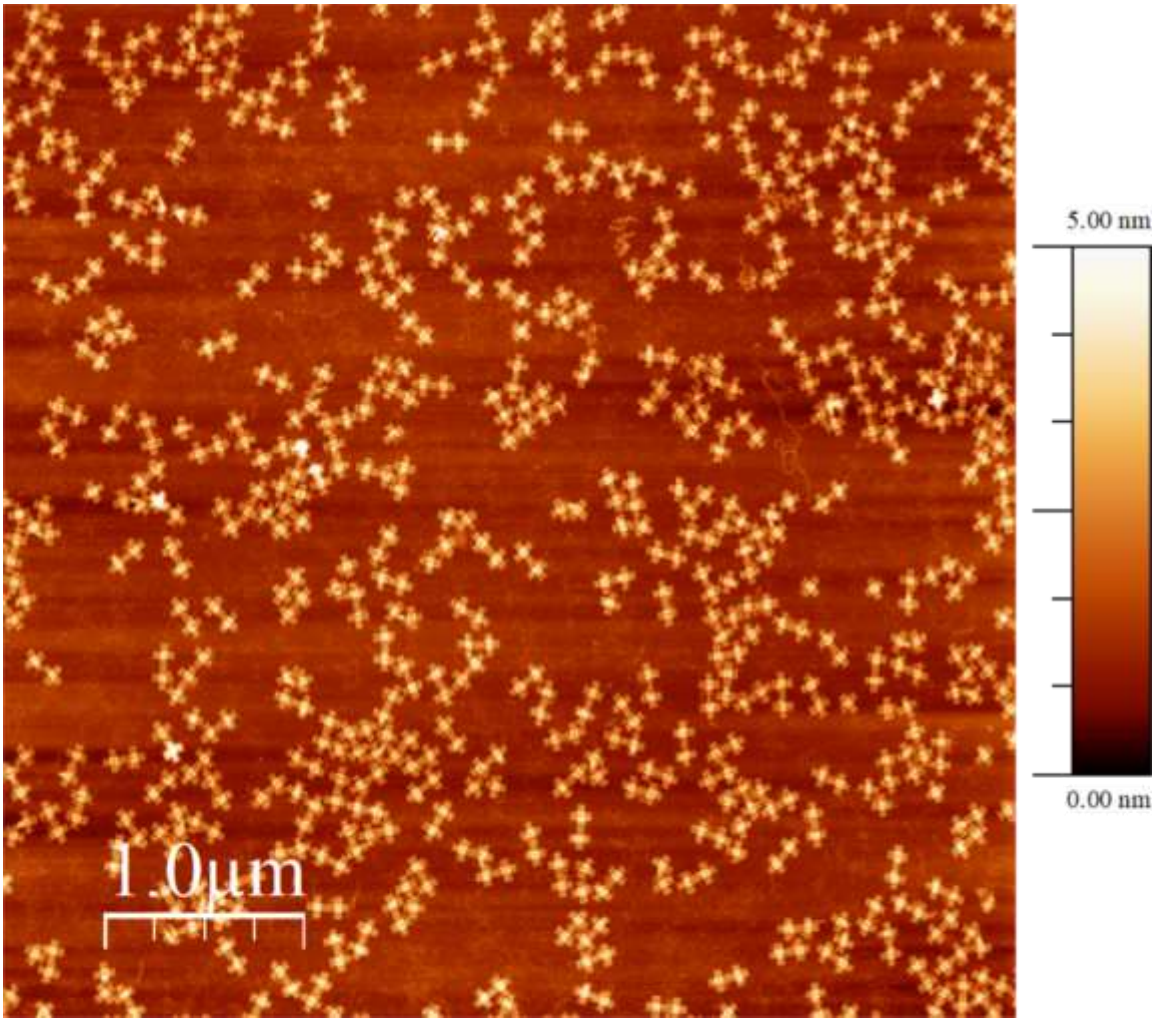

Figure 2.5: Atomic force microscope (AFM) image of DNA origami dimers on mica. Each structure was imaged with AFM to confirm the formation of origami cross-tile dimers before SRM measurements[13].

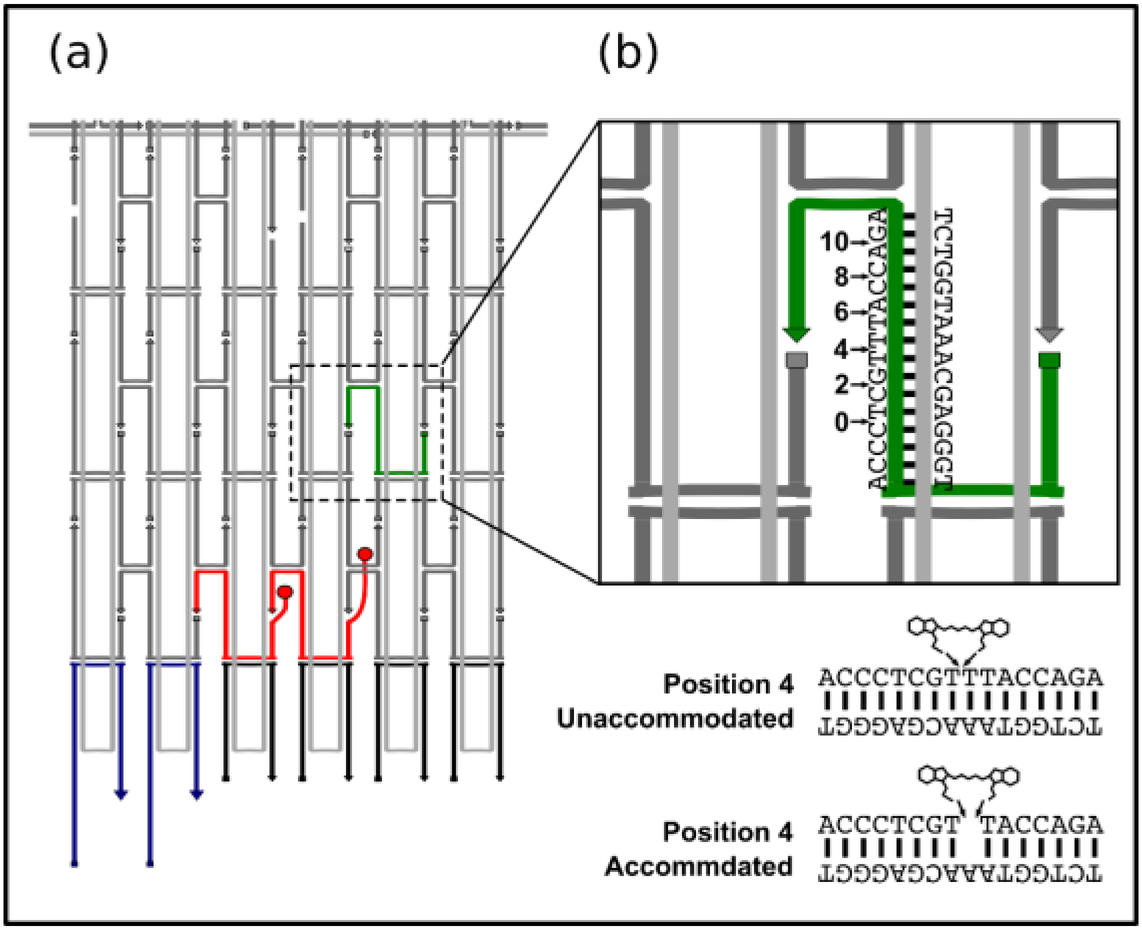

Figure 2.6: Diagram of the staple routing for the origami cross-tile A-Tile down arm. (a) Modified staples on this arm are biotin strands (red, present but unused), poly-T blocking edge strands (black), Docking Site 2 extended edge staples (blue), and the internal dye modified strand (green). (b) The numbers along the middle section of the green staple indicate the position of the dye molecule along the helix. The sequence of the middle dsDNA section is shown, and the sequences for each staple variant are given in Tables 2.15 and 2.16. Positions 0 and 10 are separated by a full helical turn, 10 base pairs, and are on the substrate side of the helix when the structure is in a 'face-up' configuration. The two variants for dye position 4 are shown at the bottom.

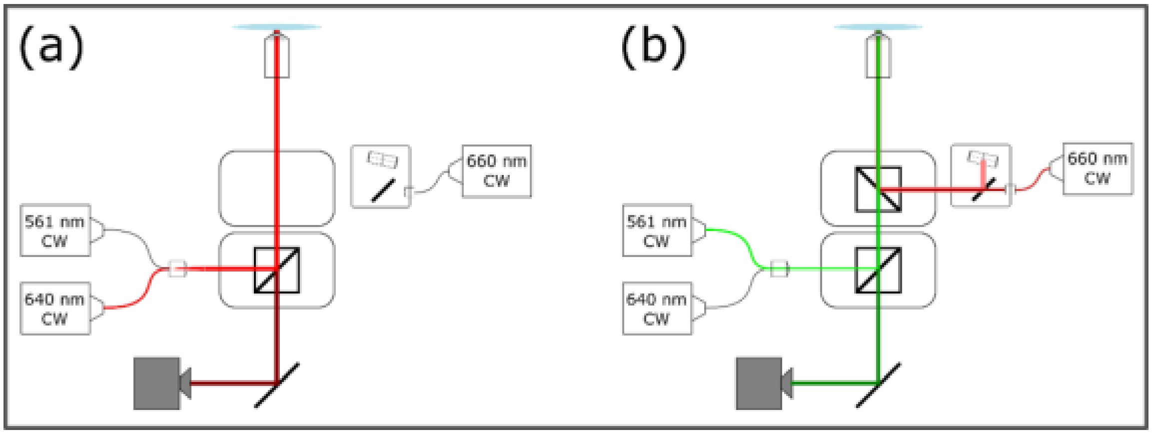

Figure 2.7: Diagram of the optical system used for sequential dipole and SRM imaging. (a) Microscope configuration when imaging fixed dipoles. Dipoles are imaged first to reduce the photoinduced bleaching from exposure to the 660 nm laser used by the custom real-time z-drift correction system built in-house and required for SRM. This overlap in wavelengths means that the z-drift system is off during dipole imaging. (b) Microscope configuration after switching to SRM with Cy3b immediately following dipole imaging. A short pass dichroic mirror is placed in the beam path in the upper turret to allow for real-time z-drift correction during the long imaging times required for SRM.

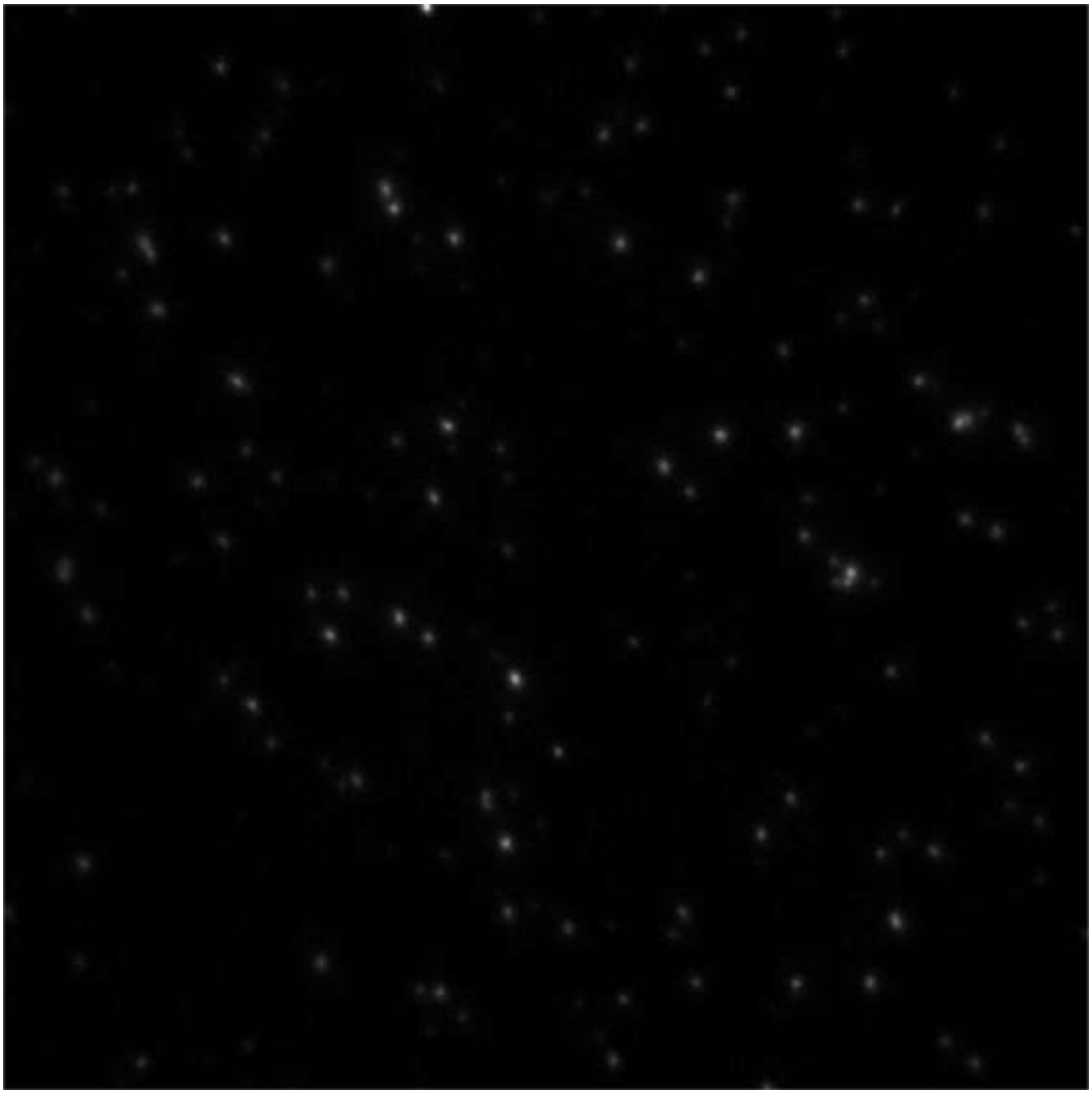

Figure 2.8: Raw image capture of diIC2(5) phosphoramidite dipole emission patterns. Image dimensions are 55 x 55 µm^2 with a 512 x 512 pixel ROI and a defocus = 200 nm. The image also contains defocused AuNPs.

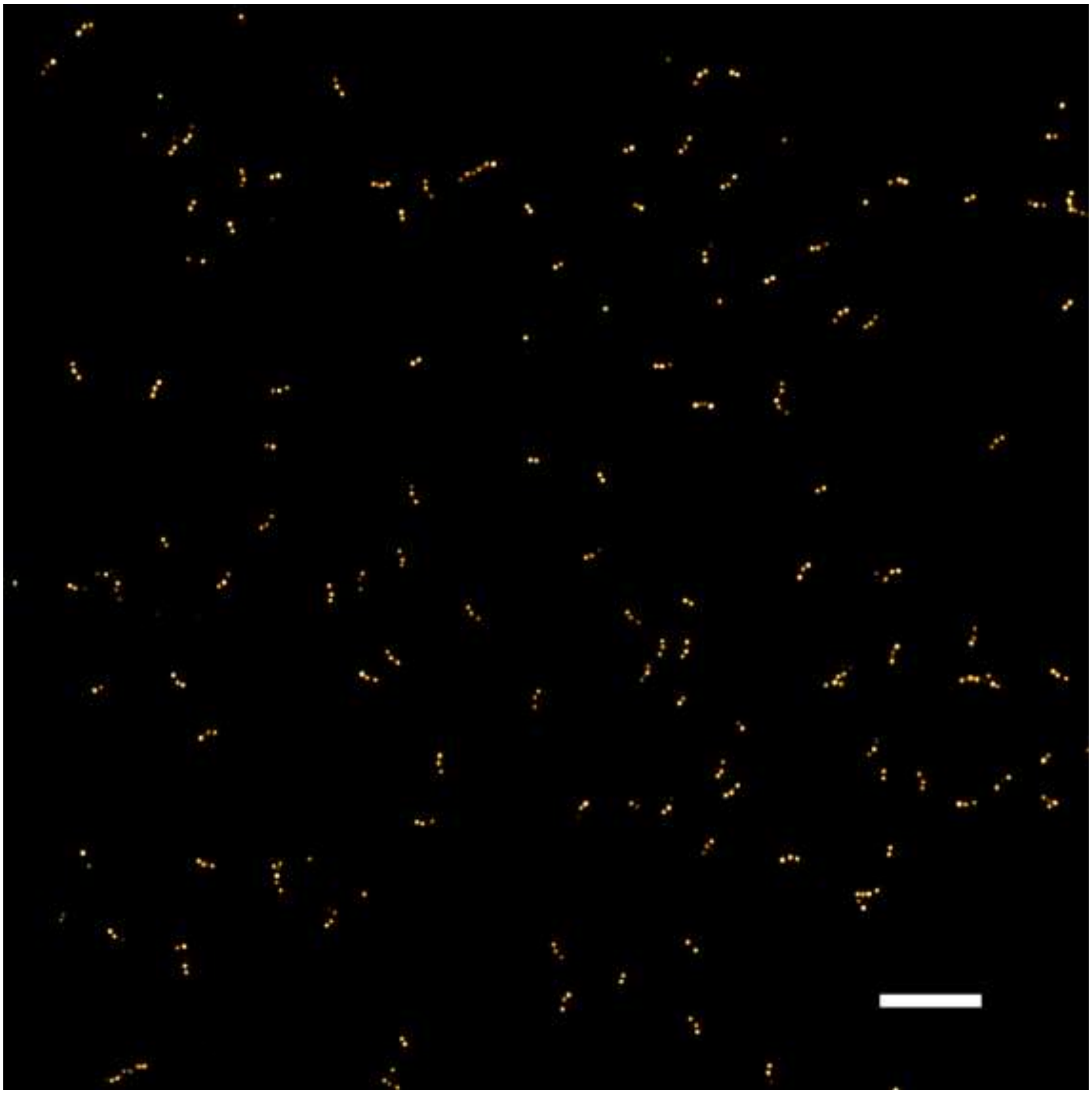

Figure 2.9: Super-resolution image of Docking Site 1 localizations. This image is 1/5 of the full FOV capture with a resolution of ~20 nm. Scale bar = 1 μm.

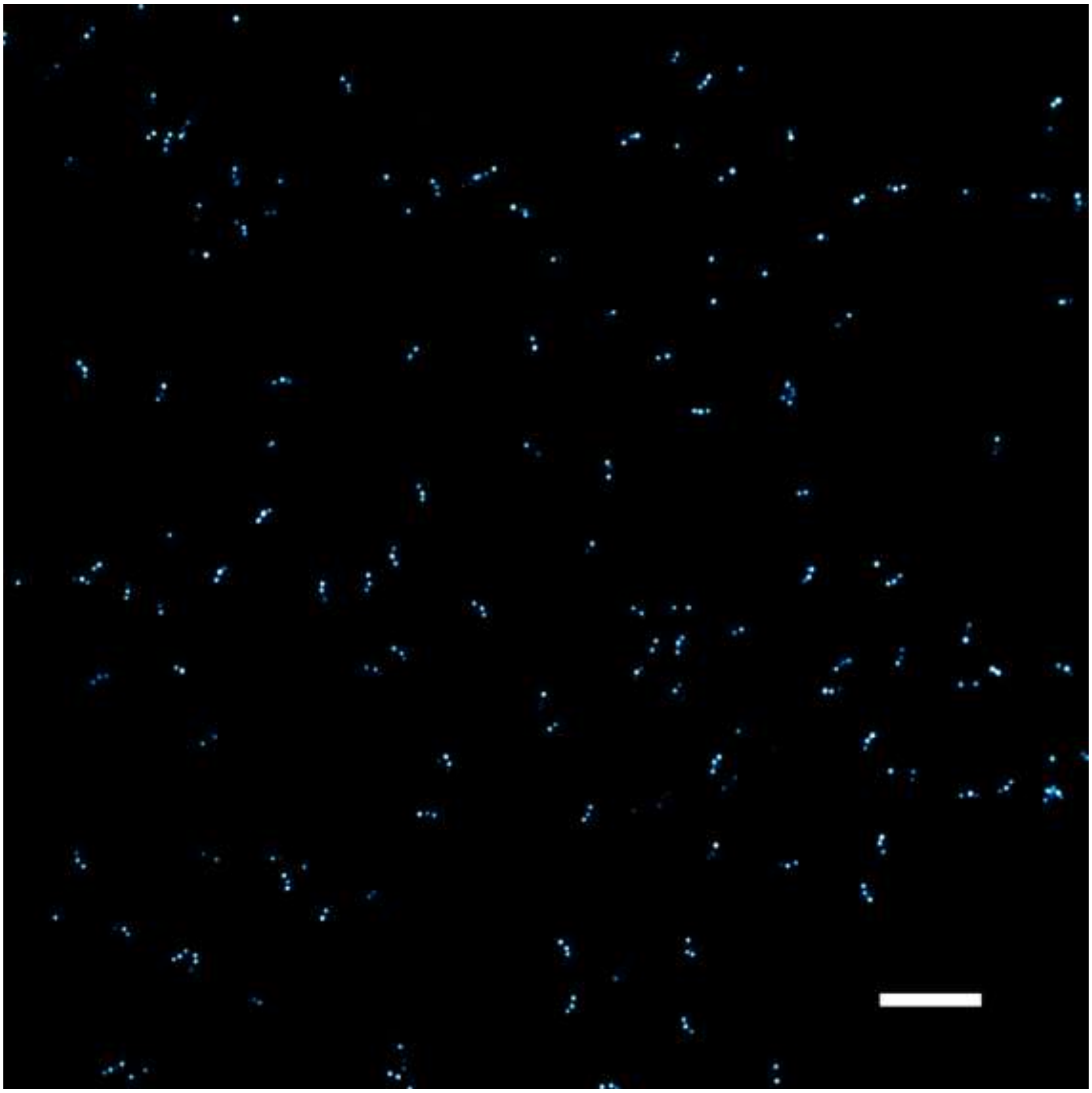

Figure 2.10: Super-resolution image of Docking Site 2 localizations. Imaging area is the same as that shown in Figure 2.9. Scale bar = 1 mm.

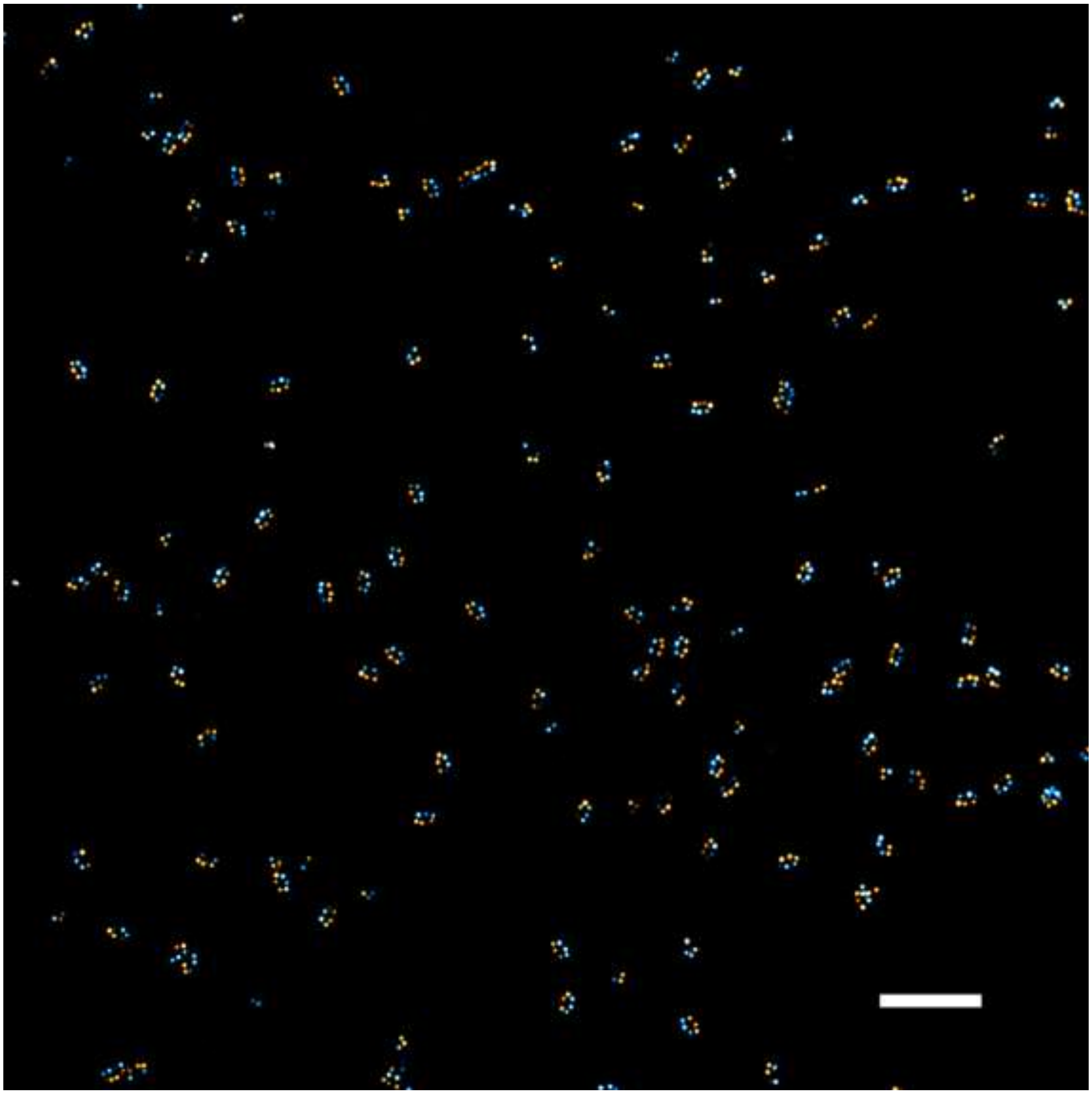

Figure 2.11: Two channel registered SRM image. Composite image comprised of the Docking Site 1 image in Figure 2.9 and the Docking Site 2 image in Figure 2.10. The two images are registered using multiple fixed gold nanoparticles found within each full frame (not shown). Scale bar = 1 μm.

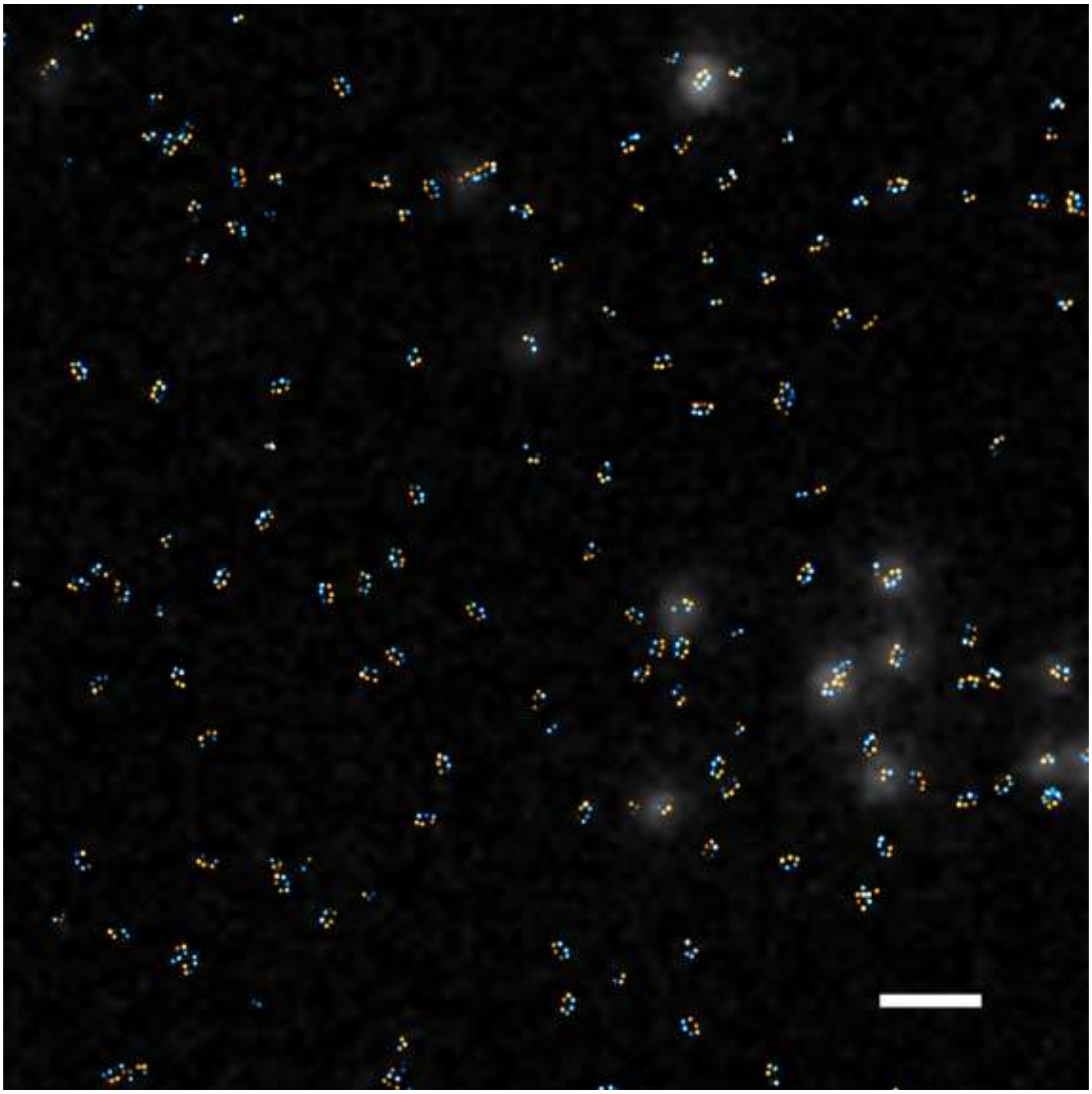

Figure 2.12: Three channel registered fluorescence microscopy image. The sm-dipole emission image taken of the same sample area as both SRM images is enlarged to match the dimensions of the SRM images and registered to the two-channel image in Figure 2.11 using the same fixed gold nanoparticles. sm-dipole emission patterns (shown as white halos, contrast enhanced for visibility) can now be attributed to specific origami structures when origami is sufficiently dispersed. Scale bar = 1 μm.

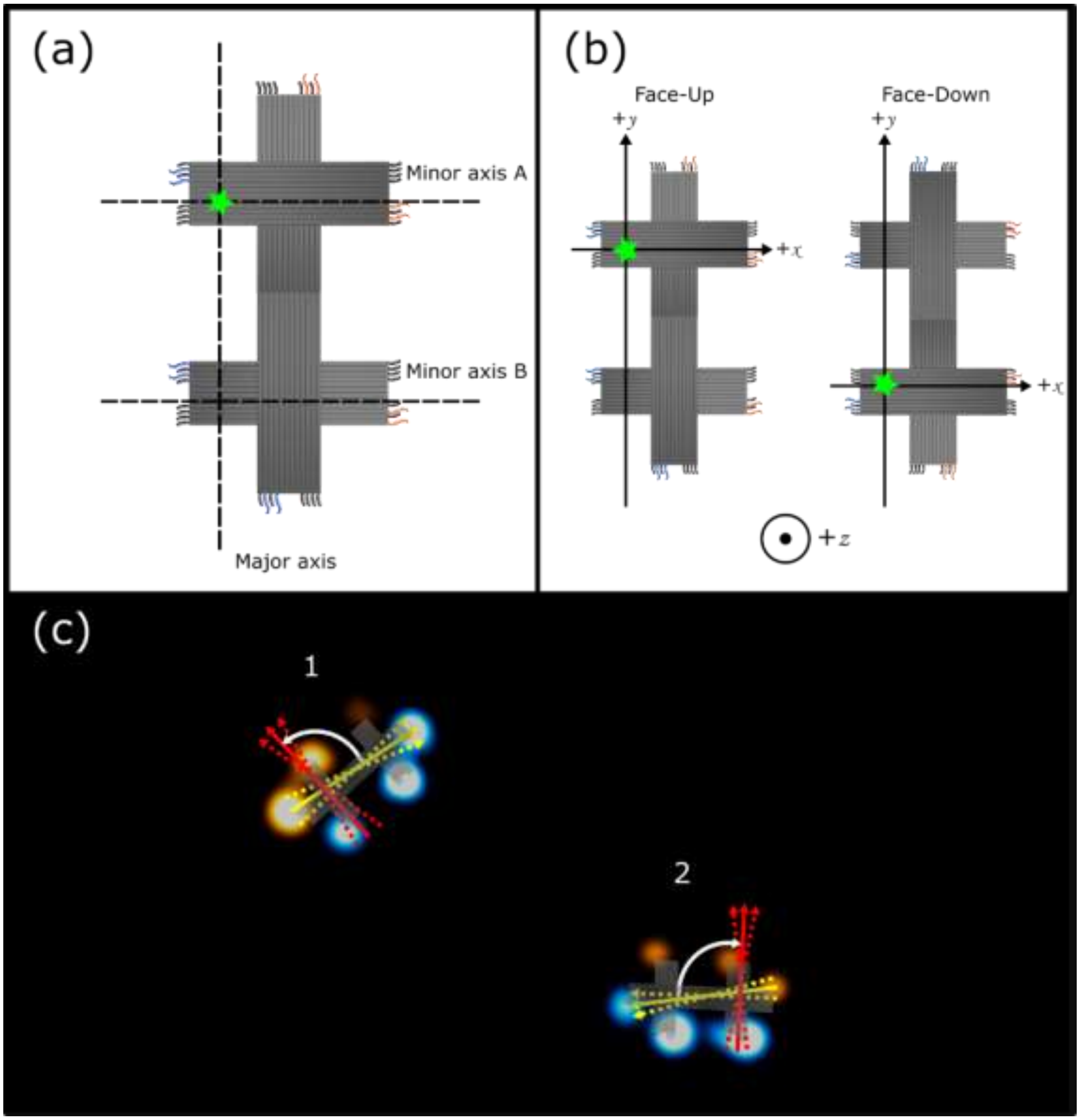

Figure 2.13: Determining orientations of the helical domains of the dsDNA substrates. (a) Schematic of a DNA origami cross-tile with the major and minor axes defined (dashed black lines). (b) Origami cross-tiles overlaid on Cartesian coordinate systems in the 'face-up' and 'face-down' orientations. With the +z-axis coming out of the page and Docking Sites 1 (orange extended strands) on the minor axes always in the +x direction, the two faces are differentiated by the locations of Docking Site 1 on the major axis being in the +y (face-up) or –y (face-down) direction according to the RHR. (c) Two channel SRM image of origami dimers in face-up (1) and face-down (2) orientations. The orientation of the minor axis A (red solid arrow) can be calculated (white arcs) from the measured orientation of the major axis (solid yellow arrow). The upper and lower bounds of the origami orientation (red dashed arrows) are measured from the uncertainty of the localizations (yellow dashed arrows).

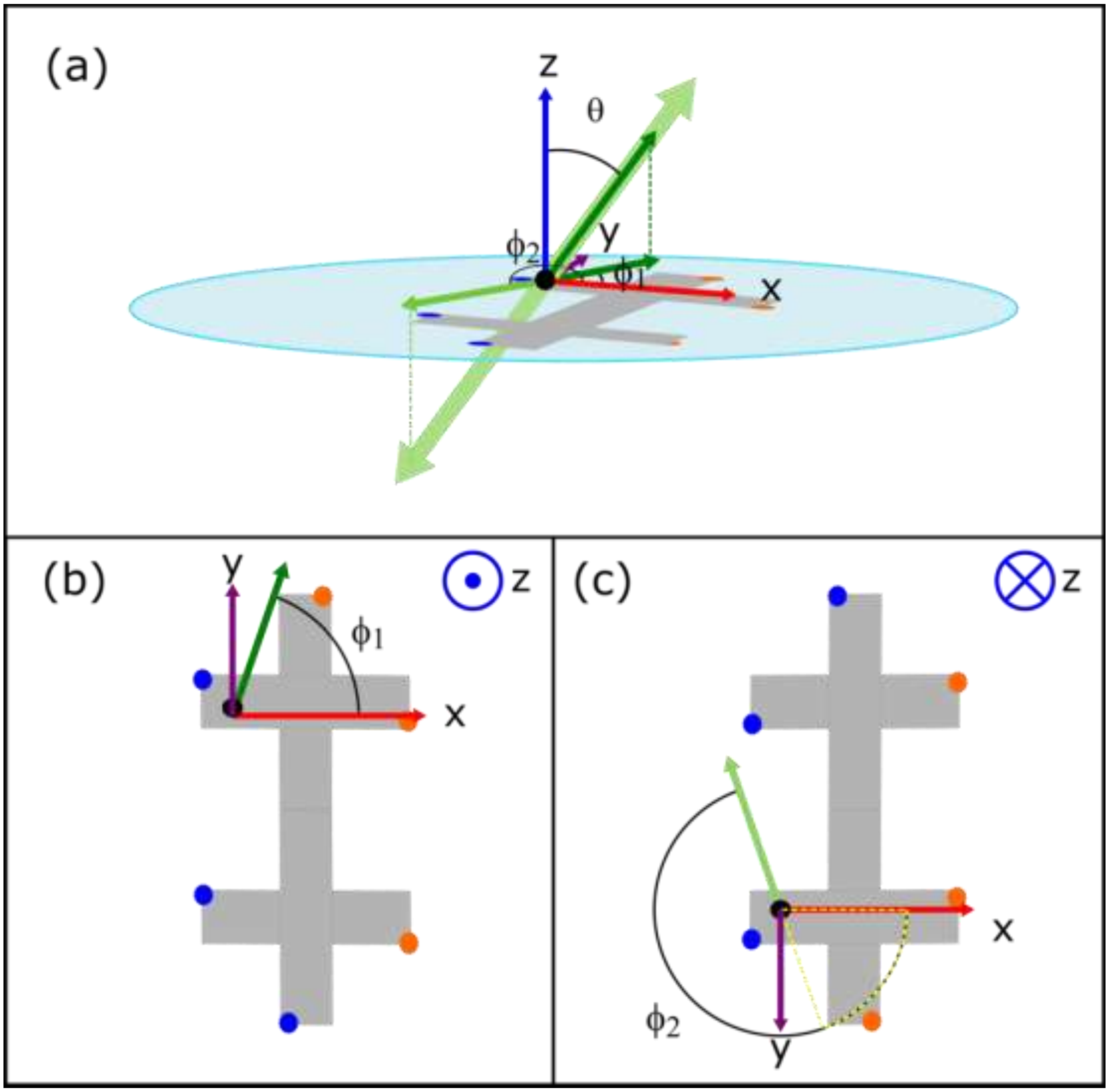

Figure 2.14: Schematic showing the measured relative angle of a dipole to the DNA substrate depending on the landing orientation of the origami. To be consistent in our data, all orientations are reported relative to an origami dimer that has landed face up. (a) A 3D schematic of dipole above an interface and its projection on the 2D plane (dark green arrows) with a specific orientation of (θ, ϕ_1) relative to the DNA substrate which is in the face-up orientation. The entire dipole is shown in light green as it exists in real space along with the 2D projection of the end of dipole below the interface with ϕ_2. (b) Measuring ϕ_1 relative to a face up origami is straight forward: looking down from +z (blue point), measuring from +x axis (red arrow) toward the +y axis (purple arrow) to the dark green dipole projection. (c) When we encounter a face-down origami as defined in Figure 2.13b with an identical dipole orientation in real space relative to the DNA substrate, we know from (a) that we can reorient our coordinate system so that instead of looking at a face down origami from the +z direction, we can think of it as a face up origami from the –z direction (blue cross) and ϕ_2 measured in this revised coordinate system from +x axis toward +y axis to the light green projection is ϕ_1 (yellow section) + 180°.

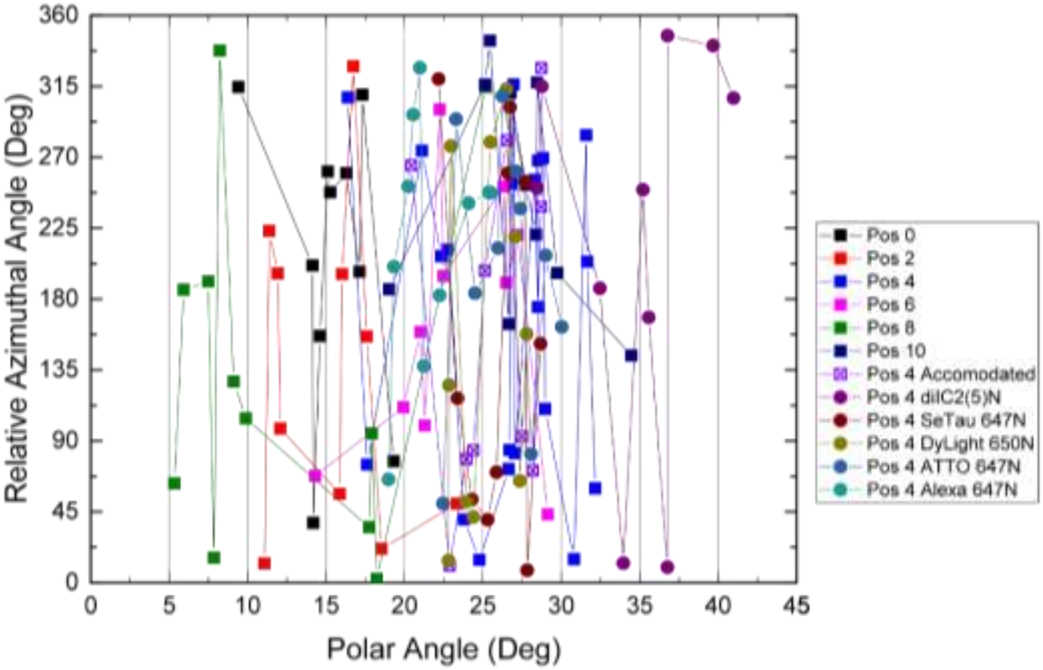

Figure 2.15: Relative azimuthal (ϕ) vs polar (θ) angle of each measured dipole. Plotting the component angles of each measured dipole illustrates the large variation in relative azimuthal angle observed for each dye position and the lower variation in polar angle.

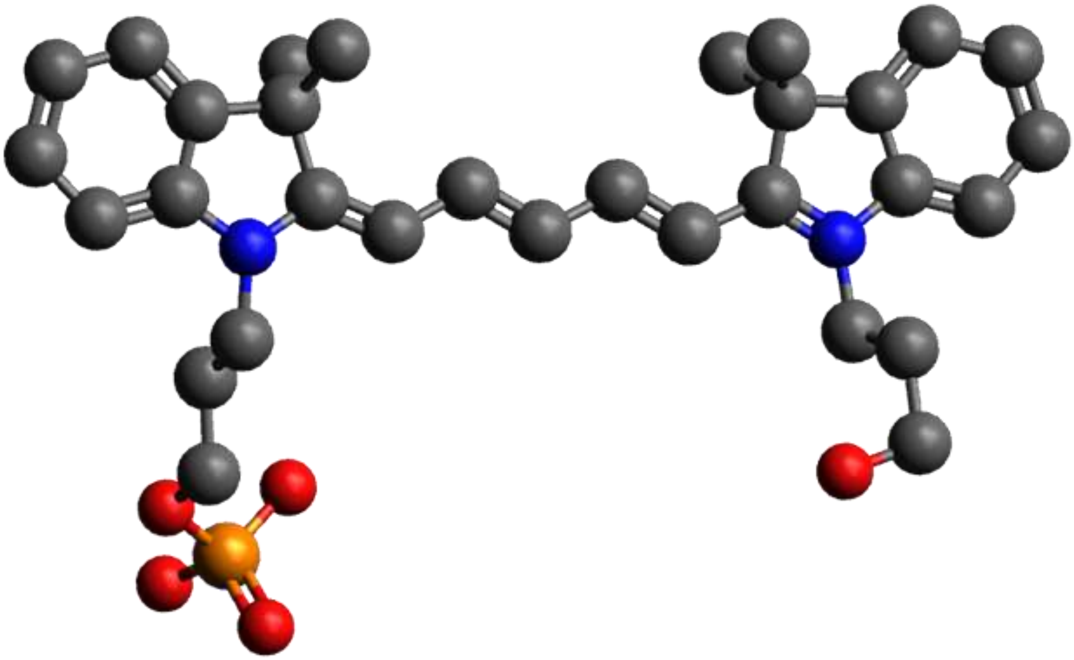

Figure 2.16: Structure of phosphoramidite diIC2(5). An atomic model of the phosphoramidite diIC2(5) molecule, generated in Avogadro 1.2, which is embedded in an ssDNA oligo to form an internally modified DNA origami staple strand. Carbon atoms shown in gray, nitrogen atoms in blue, oxygen atoms in red, phosphorus in orange, and hydrogens not shown.

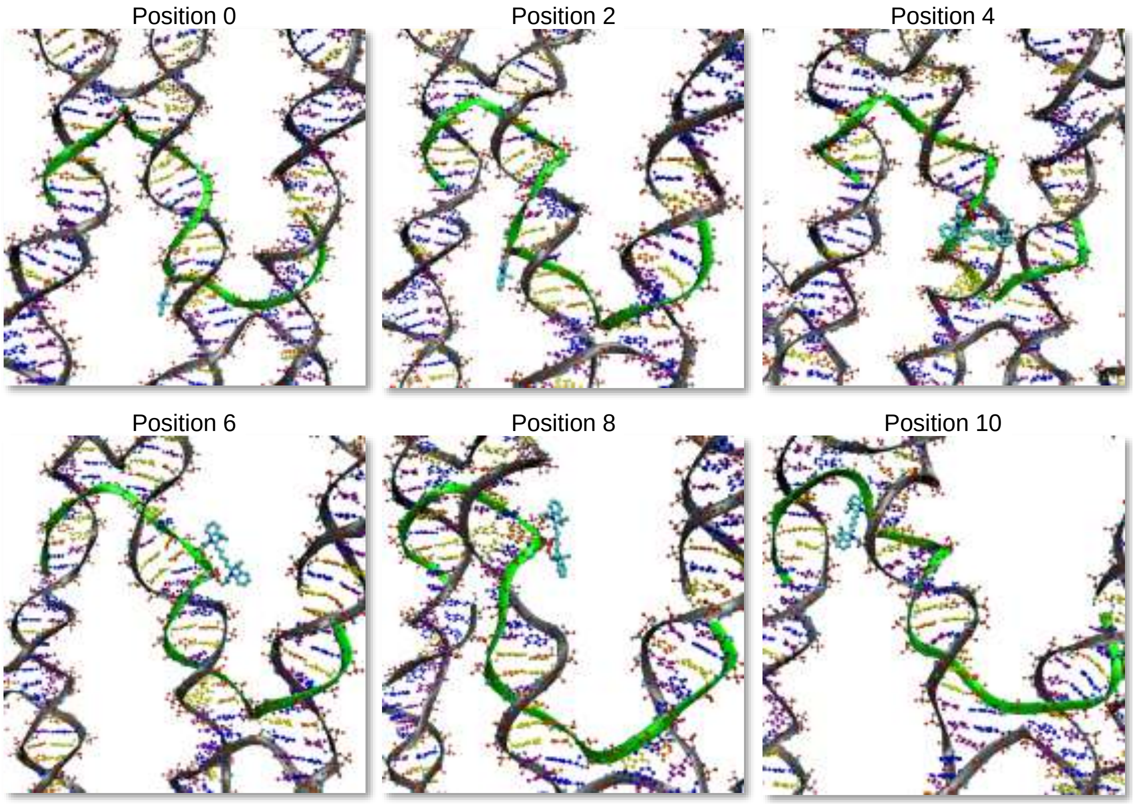

Position 0

Position 2

Position 4

Position 6

Position 8

Position 10

Figure 2.17: NAMD Structures for diIC2(5) Phosphoramidite. Atomic models illustrating the location of the diIC2(5) phosphoramidite at positions 0 to 10 of the modified full sequence staple strand. All models are shown in the "face-up" orientation.

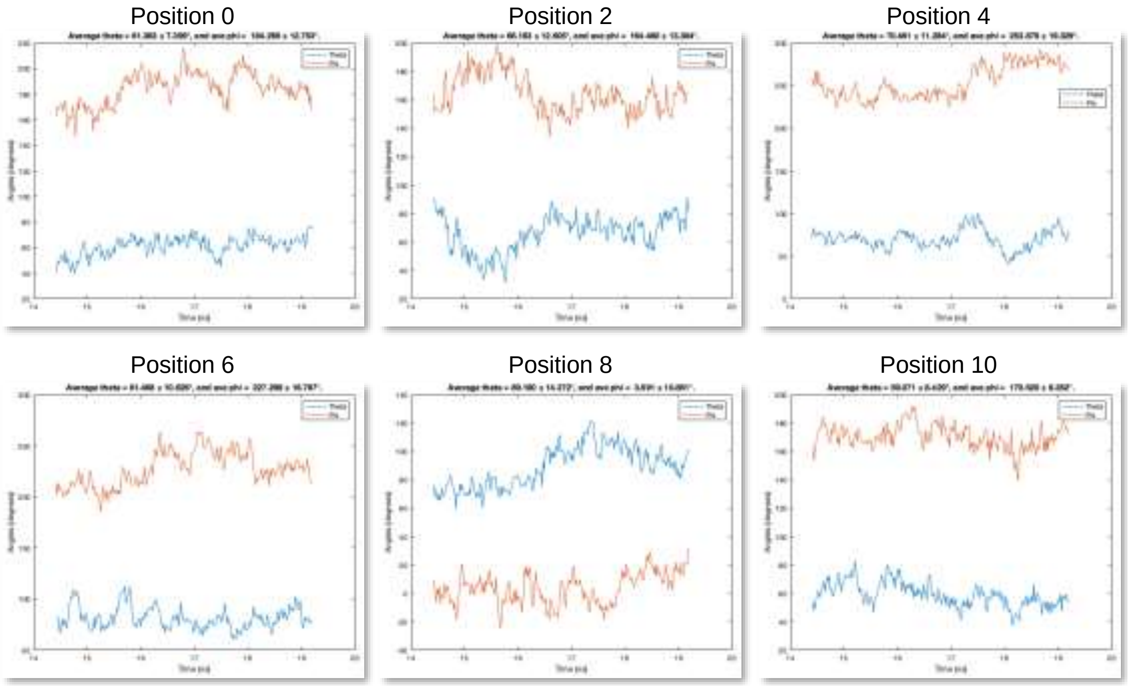

Figure 2.18: NAMD Orientations for diIC2(5) Phorphoramidite. Theta and phi angles for diIC2(5) phosphoramidite at positions 0 to 10 of the modified full sequence staple strand. Angles were computed using the coordinates of the diIC2(5) nitrogen atoms in each frame of the fully relaxed NAMD simulation (final 4.8 ns).

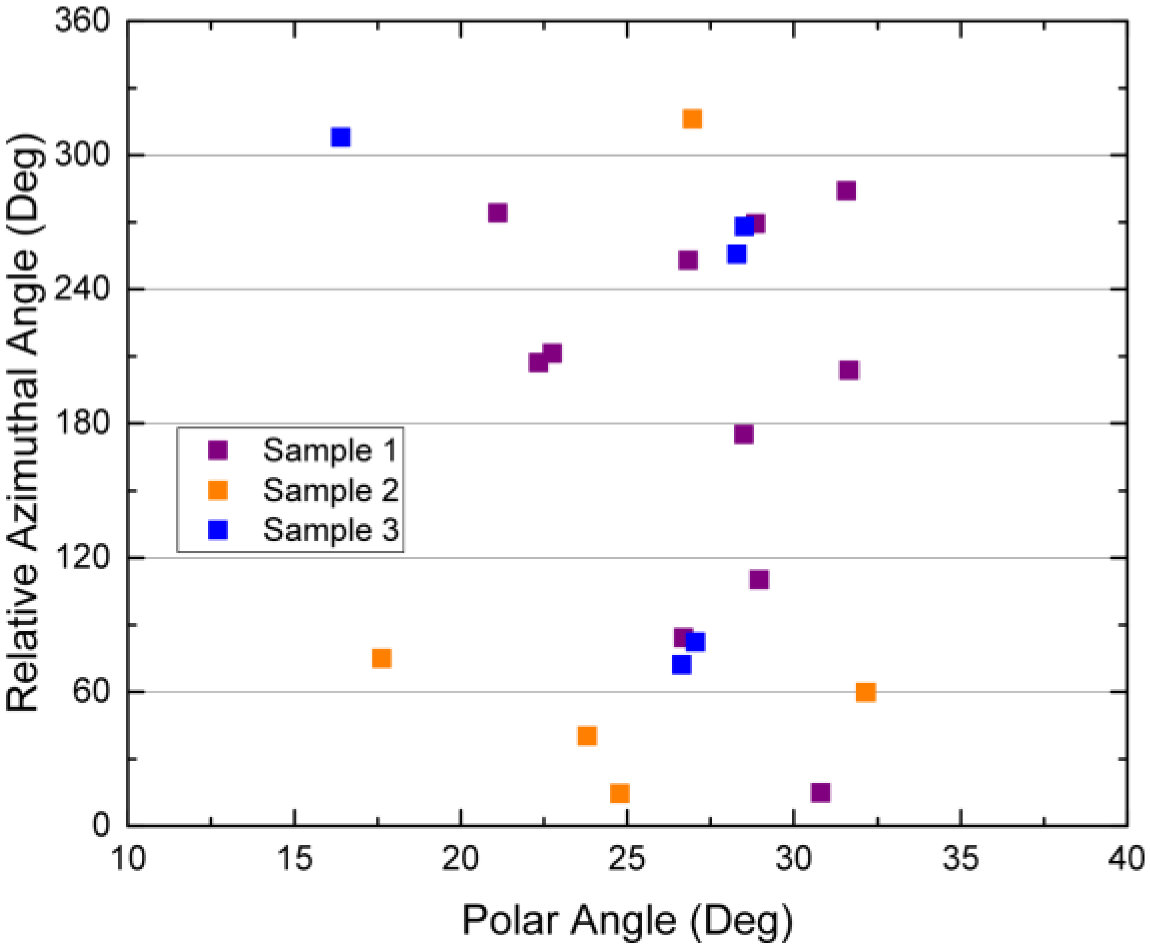

Figure 2.19: Relative Azimuthal vs Polar Angles of each measured diIC2(5) dipole molecule at dye position 4. Sample 1 was imaged at a defocus of 200 nm. Samples 2 and 3 were each prepared nine months later from the same stock as Sample 1 and imaged at a defocus of 200 nm and 600 nm, respectively.

2.8.4 Supplementary Tables

Table 2.1: Measured orientations of embedded diIC2(5) molecules at dye position 0 relative to dsDNA substrate

Structure	θ (°)	φ (°)
1	14.2	38.0 ± 9.8
2	17.3	309.6 ± 7.5
3	14.1	201.3 ± 7.4
4	17.1	197.3 ± 8.0
5	16.3	259.8 ± 7.4
6	19.3	77.0 ± 11.1
7	15.3	247.8 ± 7.3
8	14.6	156.6 ± 8.3
9	9.4	314.7 ± 7.8
10	15.1	260.9 ± 7.7

Table 2.2: Measured orientations of embedded diIC2(5) molecules at dye position 2 relative to dsDNA substrate

Structure	θ (°)	φ (°)
1	23.3	50.1 ± 8.3
2	11.1	12.3 ± 9.1
3	11.9	196.3 ± 14.4
4	11.4	223.2 ± 12.1
5	16.0	195.8 ± 9.0
6	12.1	97.8 ± 9.6
7	16.7	327.8 ± 12.0
8	15.9	56.5 ± 8.8
9	17.6	156.3 ± 13.6
10	18.5	21.5 ± 13.4

Table 2.3: Measured orientations of embedded diIC2(5) molecules at dye position 4 relative to dsDNA substrate

Structure	θ (°)	φ (°)
1	30.8	14.8 ± 7.2
2	26.8	253.0 ± 9.3
3	22.3	207.1 ± 7.8
4	31.6	284.0 ± 10.5
5	28.5	175.0 ± 7.0
6	21.1	274.1 ± 7.8
7	28.9	269.4 ± 11.2
8	31.7	203.8 ± 7.2
9	22.8	211.3 ± 9.1
10	26.7	84.2 ± 8.8
11	29.0	110.2 ± 8.3
12	16.4	307.9 ± 8.8
13	28.3	255.7 ± 16.5
14	27.1	82.3 ± 9.0
15	26.6	72.2 ± 20.6
16	28.5	268.0 ± 15.1
17	27.0	316.2 ± 8.45
18	17.6	75.0 ± 7.4
19	32.2	59.8 ± 9.1
20	24.8	14.5 ± 7.9
21	23.8	40.2 ± 11.6

Table 2.4: Measured orientations of embedded diIC2(5) molecules at dye position 6 relative to dsDNA substrate

Structure	θ (°)	φ (°)
1	26.3	251.4 ± 9.4
2	19.9	111.3 ± 9.2
3	14.3	67.7 ± 9.0
4	22.2	300.3 ± 8.9
5	27.2	220.7 ± 14.8
6	21.0	159.0 ± 10.7
7	22.5	194.6 ± 7.4
8	21.3	99.7 ± 5.7
9	26.5	190.5 ± 9.6
10	29.1	43.4 ± 7.3

Table 2.5: Measured orientations of embedded diIC2(5) molecules at dye position 8 relative to dsDNA substrate

Structure	**θ (°)**	**φ (°)**
1	7.5	191.1 ± 6.2
2	5.3	63.0 ± 4.5
3	7.9	15.8 ± 8.9
4	9.9	104.2 ± 6.7
5	25.2	314.7 ± 6.5
6	18.2	2.4 ± 6.2
7	5.9	186.0 ± 7.1
8	17.7	35.2 ± 7.6
9	17.9	94.7 ± 9.8
10	9.1	127.6 ± 11.1
11	8.2	337.6 ± 10.9

Table 2.6: Measured orientations of embedded diIC2(5) molecules at dye position 10 relative to dsDNA substrate

Structure	**θ (°)**	**φ (°)**
1	25.4	344.0 ± 7.5
2	28.4	220.9 ± 7.4
3	26.8	310.7 ± 9.2
4	29.7	196.5 ± 10.2
5	26.7	164.3 ± 7.8
6	27.8	252.3 ± 6.7
7	19.0	186.2 ± 6.1
8	28.5	317.4 ± 9.2
9	34.5	144.2 ± 5.0
10	25.1	316.1 ± 7.6

Table 2.7: Measured orientations of embedded diIC2(5) molecules opposite an unpaired base relative to dsDNA substrate

Structure	θ (°)	φ (°)
1	28.2	71.1 ± 5.9
2	25.1	198.0 ± 7.3
3	28.7	326.7 ± 5.9
4	22.9	10.8 ± 5.6
5	24.0	78.4 ± 5.2
6	26.5	280.7 ± 9.5
7	24.4	83.9 ± 4.5
8	28.7	238.7 ± 7.2
9	20.4	264.8 ± 9.8
10	27.5	92.7 ± 5.3

Table 2.8: Measured orientations of embedded diIC2(5)N molecules at dye position 5 relative to dsDNA substrate. Position 5 is shifted by one thymine toward position 6.

Structure	θ (°)	φ (°)
1	28.8	315.0 ± 9.8
2	35.2	249.3 ± 4.3
3	34.0	12.3 ± 10.7
4	36.8	347.2 ± 6.6
5	36.8	9.8 ± 9.7
6	41.0	307.5 ± 11.0
7	39.7	340.9 ± 7.8
8	35.6	168.3 ± 11.0
9	32.5	186.7 ± 7.1
10	28.5	250.4 ± 7.9

Table 2.9: Measured orientations of embedded SeTau 647N molecules at dye position 4 relative to dsDNA substrate

Structure	θ (°)	φ (°)
1	27.7	254.6 ± 10.0
2	28.7	151.6 ± 8.6
3	25.9	70.1 ± 13.4
4	27.8	7.8 ± 6.8
5	23.4	116.9 ± 5.8
6	26.7	301.7 ± 6.9
7	25.3	40.0 ± 8.5
8	24.3	52.8 ± 7.3
9	26.6	259.9 ± 6.3
10	22.2	319.7 ± 9.6

Table 2.10: Measured orientations of embedded DyLight 650N molecules at dye position 4 relative to dsDNA substrate

Structure	θ (°)	φ (°)
1	23.0	277.1 ± 9.3
2	27.4	64.6 ± 6.2
3	22.8	125.3 ± 6.3
4	27.8	157.9 ± 6.6
5	22.8	14.0 ± 8.4
6	25.5	279.6 ± 6.4
7	26.5	313.2 ± 8.8
8	27.1	219.5 ± 9.1
9	24.4	41.7 ± 8.3
10	23.9	51.2 ± 8.2

Table 2.11: Measured orientations of embedded ATTO 647N molecules at dye position 4 relative to dsDNA substrate

Structure	**θ (°)**	**φ (°)**
1	27.1	261.0 ± 10.1
2	28.1	81.6 ± 6.5
3	23.3	294.1 ± 7.5
4	22.5	50.2 ± 7.4
5	24.5	183.8 ± 9.7
6	26.0	212.4 ± 10.0
7	29.0	207.7 ± 7.9
8	27.4	237.4 ± 9.6
9	30.0	162.3 ± 7.2
10	26.2	308.8 ± 6.7

Table 2.12: Measured orientations of embedded Alexa 647N molecules at dye position 4 relative to dsDNA substrate

Structure	**θ (°)**	**φ (°)**
1	25.4	247.7 ± 8.8
2	21.0	326.8 ± 6.7
3	24.1	240.8 ± 7.7
4	25.5	247.5 ± 7.6
5	22.2	182.3 ± 8.4
6	20.6	297.0 ± 4.1
7	19.3	200.6 ± 11.8
8	21.2	137.4 ± 10.6
9	20.2	251.5 ± 5.9
10	19.0	65.5 ± 7.1

Table 2.13: Cross-Tile Staple Strand List (A-Tile Edge Staples)

Name	Sequence	Notes
CO-A-L1	TCCTGAACAAGAAAAAATCAACAATAGATAAGAATACATCT	Docking Site 1
CO-A-L2	TTGCACCCAGCTACAAAAGATTAGTTGCTATTAATACATCT	Docking Site 1
CO-A-L3	TTTTTTAATAATAAGAGCAAGAGAATTGAGTTAAGCCCTTTTTT	Blocking
CO-A-L4	TTTTTTGTTTGAGGGGACGACGAACCGTGCATCTGCCATTTTTT	Blocking
CO-A-L5	TTTTTTCCCGGGTACCGAGGTCTCGACTCTAGAGGATC	Blocking
CO-A-L6	TTTTTTAGCTGATTGCCCTTCACAGTGAGACGGGCAAC	Blocking
CO-A-U1	AATAAGTTTATTTTGTCGCAAAGACACCACGGTTTTTT	Blocking
CO-A-U2	TGTAGCGCGTTTTCATGCCTTTAGCGTCAGACTTTTTT	Blocking
CO-A-U3	TTTTTTAATTTACCGTTCCAGTGAAAGCGCAGTCTCTGTTTTTT	Blocking
CO-A-U4	TTTTTTGGTTTAGTACCGCCACATCACCGTACTCAGGATTTTTT	Blocking
CO-A-U5	ACTAAAGGAATTGCGAAGAATAGAAAGGAACAAATACATCT	Docking Site 1
CO-A-U6	GAGGACTAAAGACTTTCGGCTACAGAGGCTTTAATACATCT	Docking Site 1
CO-A-R1	CTGTTGTTAAATAAGAATAAAGTGTGATAAATAAGGC	Sticky-end
CO-A-R2	CGAATAAATCGTCGCTATTAAATAACCTTGCTTCTGT	Sticky-end
CO-A-R3	GTCTTAAATAAAGAAATTGCGTTAGCACGTAAAACAGAAGGT	Sticky-end
CO-A-R4	ATCCTTATTCCTGATTATCAGAGCGGAATTATCATCATATGG	Sticky-end
CO-A-R5	TGCTGAACCTCAAATAATCTAAAGCATCACCTGCAAA	Sticky-end
CO-A-R6	ACATTGGCAGATTCACCTGAAATGGATTATTTAGCAT	Sticky-end
CO-A-D1	CGTTAATATTTTGTTAATATTTAAATTGTAAAAAAGGTATC	Docking Site 2
CO-A-D2	TGAGTAATGTGTAGGTTTTTAAATGCAATGCCAAAGGTATC	Docking Site 2
CO-A-D3	TTTTTTATTAGATACATTTCGCTAGATTTAGTTTGACCTTTTTT	Blocking
CO-A-D4	TTTTTTATCAAAAAGATTAAGAAAGCAAAGCGGATTGCTTTTTT	Blocking
CO-A-D5	ATAACGCCAAAAGGAACAACTAATGCAGATACTTTTTT	Blocking
CO-A-D6	GGATATTCATTACCCAATCTTCGACAAGAACCTTTTTT	Blocking

Table 2.14: Cross-Tile Staple Strand List (B-Tile Edge Staples)

Name	Sequence	Notes
CO-B-L1	AACAGCGTTAATATTTTGTTAATATTTAAATTGTAAA	Sticky-end
CO-B-L2	ATTCGTGAGTAATGTGTAGGTTTTTAAATGCAATGCC	Sticky-end
CO-B-L3	AAGACATTAGATACATTTCGCTAGATTTAGTTTGACCACCTT	Sticky-end
CO-B-L4	AGGATATCAAAAAGATTAAGAAAGCAAAGCGGATTGCCCATA	Sticky-end
CO-B-L5	ATAACGCCAAAAGGAACAACTAATGCAGATACTTTGC	Sticky-end
CO-B-L6	GGATATTCATTACCCAATCTTCGACAAGAACCATGCT	Sticky-end
CO-B-U1	TCCTGAACAAGAAAAAATCAACAATAGATAAGAATACATCT	Docking Site 1
CO-B-U2	TTGCACCCAGCTACAAAAGATTAGTTGCTATTAATACATCT	Docking Site 1
CO-B-U3	TTTTTTAATAATAAGAGCAAGAGAATTGAGTTAAGCCCTTTTTT	Blocking
CO-B-U4	TTTTTTGTTTGAGGGGACGACGAACCGTGCATCTGCCATTTTTT	Blocking
CO-B-U5	TTTTTTCCCGGGTACCGAGGTCTCGACTCTAGAGGATC	Blocking
CO-B-U6	TTTTTTAGCTGATTGCCCTTCACAGTGAGACGGGCAAC	Blocking
CO-B-R1	AATAAGTTTATTTTGTCGCAAAGACACCACGGTTTTTT	Blocking
CO-B-R2	TGTAGCGCGTTTTCATGCCTTTAGCGTCAGACTTTTTT	Blocking
CO-B-R3	TTTTTTAATTTACCGTTCCAGTGAAAGCGCAGTCTCTGTTTTTT	Blocking
CO-B-R4	TTTTTTGGTTTAGTACCGCCACATCACCGTACTCAGGATTTTTT	Blocking
CO-B-R5	ACTAAAGGAATTGCGAAGAATAGAAAGGAACAAAAGGTATC	Docking Site 2
CO-B-R6	GAGGACTAAAGACTTTCGGCTACAGAGGCTTTAAAGGTATC	Docking Site 2
CO-B-D1	TTTTTTGTTAAATAAGAATAAAGTGTGATAAATAAGGC	Blocking
CO-B-D2	TTTTTTAAATCGTCGCTATTAAATAACCTTGCTTCTGT	Blocking
CO-B-D3	TTTTTTAAATAAAGAAATTGCGTTAGCACGTAAAACAGTTTTTT	Blocking
CO-B-D4	TTTTTTTATTCCTGATTATCAGAGCGGAATTATCATCATTTTTT	Blocking
CO-B-D5	TGCTGAACCTCAAATAATCTAAAGCATCACCTAAAGGTATC	Docking Site 2
CO-B-D6	ACATTGGCAGATTCACCTGAAATGGATTATTTAAAGGTATC	Docking Site 2

Table 2.15: Cross-Tile Staple Strand List (Internal diIC2(5) Modified Strands)

Name	Sequence	Notes
CO-M-106-diIC2(5)-0	GTAGAAAG-ACCC/iCy5/TCGTTTACCAGA-ATGACCAT	Dye position 0
CO-M-106-diIC2(5)-2	GTAGAAAG-ACCCTC/iCy5/GTTTACCAGA-ATGACCAT	Dye position 2
CO-M-106-diIC2(5)-4	GTAGAAAG-ACCCTCGT/iCy5/ TTACCAGA-ATGACCAT	Dye position 4
CO-M-106-diIC2(5)-6	GTAGAAAG-ACCCTCGTTT/iCy5/ACCAGA-ATGACCAT	Dye position 6
CO-M-106-diIC2(5)-8	GTAGAAAG-ACCCTCGTTTAC/iCy5/CAGA-ATGACCAT	Dye position 8
CO-M-106-diIC2(5)-10	GTAGAAAG-ACCCTCGTTTACCA/iCy5/GA-ATGACCAT	Dye position 10
CO-M-106-diIC2(5)-U	GTAGAAAG-ACCCTCGT/iCy5/TACCAGA-ATGACCAT	Accommodated Dye Position 4

Dashes have been added to indicate cross-over locations.

Table 2.16: Cross-Tile Staple Strand List (NHS Ester Dye Modified Strands)

Name	Sequence	Notes
CO-M-106-diIC2(5)N	GTAGAAAG-ACCCTCGTT/diIC2(5)N/ACCAGA-ATGACCAT	Dye position 5
CO-M-106-SeTau647	GTAGAAAG-ACCCTCGT/SeTau647N/TTACCAGA-ATGACCAT	Dye position 4
CO-M-106-DyLight650	GTAGAAAG-ACCCTCGT/DyLight650N/TTACCAGA-ATGACCAT	Dye position 4
CO-M-106-ATTO647	GTAGAAAG-ACCCTCGT/IATTO647N/TTACCAGA-ATGACCAT	Dye position 4
CO-M-106-Alexa647	GTAGAAAG-ACCCTCGT/Alex647N/TTACCAGA-ATGACCAT	Dye position 4

Dashes have been added to indicate cross-over locations.

Table 2.17: Imager Strand List

Name	Sequence	Notes
Imager Strand 1	CTAGATGTAT/Cy3b/	
Imager Strand 2	AGGATACCTT/Cy3b/	

2.8.5 Supplementary References

1 Green, C. M. et al. Metrology of DNA arrays by super-resolution microscopy. Nanoscale 9, 10205-10211, doi:10.1039/C7NR00928C (2017).

2 Liu, W., Zhong, H., Wang, R. & Seeman, N. C. Crystalline Two-Dimensional DNA-Origami Arrays. Angewandte Chemie International Edition 50, 264-267, doi:10.1002/anie.201005911 (2011).

3 Green, C. M. In preparation.

4 Jungmann, R. et al. Multiplexed 3D cellular super-resolution imaging with DNA-PAINT and Exchange-PAINT. Nature methods 11, 313 (2014).

5 Aguet, F., Geissbühler, S., Märki, I., Lasser, T. & Unser, M. Super-resolution orientation estimation and localization of fluorescent dipoles using 3-D steerable filters. Optics Express 17, 6829-6848, doi:10.1364/OE.17.006829 (2009).

6 Ovesný, M., Křížek, P., Borkovec, J., Švindrych, Z. & Hagen, G. M. ThunderSTORM: a comprehensive ImageJ plug-in for PALM and STORM data analysis and super-resolution imaging. Bioinformatics 30, 2389-2390 (2014).

7 Phillips, J. C. et al. Scalable molecular dynamics with NAMD. Journal of computational chemistry 26, 1781-1802 (2005).

8 Yoo, J., Li, C.-Y., Slone, S. M., Maffeo, C. & Aksimentiev, A. in DNA Nanotechnology 209-229 (Springer, 2018).

9 Douglas, S. M. et al. Rapid prototyping of 3D DNA-origami shapes with caDNAno. Nucleic Acids Research 37, 5001-5006, doi:10.1093/nar/gkp436 (2009).

10 Hanwell, M. D. et al. Avogadro: an advanced semantic chemical editor, visualization, and analysis platform. Journal of cheminformatics 4, 17 (2012).

11 Spiriti, J., Binder, J. K., Levitus, M. & Van Der Vaart, A. Cy3-DNA stacking interactions strongly depend on the identity of the terminal basepair. Biophysical journal 100, 1049-1057 (2011).

12 Snodin, B. E., Schreck, J. S., Romano, F., Louis, A. A. & Doye, J. P. Coarse-grained modelling of the structural properties of DNA origami. Nucleic acids research 47, 1585-1597 (2019).

13 Horcas, I. et al. WSXM: A software for scanning probe microscopy and a tool for nanotechnology. Review of Scientific Instruments 78, 013705, doi:10.1063/1.2432410 (2007).

CHAPTER THREE: ASSESSING THE PRECISION OF SINGLE MOLECULE CYANINE 5 PHOSPHORAMIDITE ORIENTATIONS WITHIN THE DOUBLE HELICES OF DNA FOUR-ARM JUNCTIONS IMMOBILIZED ON DNA ORIGAMI

This chapter is an article which is currently in preparation

**This chapter contains modifications from the prepared text*

3.1 Assessing the Precision of Single Molecule Cyanine 5 Phosphoramidite Orientations Within the Double Helices of DNA Four-Arm Junctions Immobilized on DNA Origami

Brett Ward[1]

Luca Piantanida[1]

Drew Lysne[1]

Elton Graugnard[1]

[1]Micron School of Materials Science and Engineering, Boise State University

Boise, Idaho USA 83725

3.2 Introduction

Self-assembly of devices and systems at the nanoscale has been a significant goal in research and manufacturing since its inception in 1959[1]. Toward this end, DNA origami has shown itself effective in positioning and orienting nanoparticles for a wide variety of possible opto-electric devices via self-assembly[2,3]. Fluorescent molecules, however, continue to present a particular challenge when control of their spatial orientation is considered[4-6]. Recently, attempts to measure the precision of orientation control for fluorescent molecules conjugated to staple strands and embedded within the double helix of DNA origami structures have revealed that the dyes exhibit a propensity to orient themselves in a semi-random nature[7]. While single molecule (sm) measurements of fluorescent molecule dipole orientations relative to their DNA origami substrates showed consistency in the polar angle among a population, the azimuthal distribution in a population of any given structure was seemingly random.

One possible source of dispersion in dipole orientations within a population of self-assembled DNA origami structures could be the numerous and complex origami folding pathways[8]. The complicated energy landscape could allow members of a seemingly identical population to possess a multitude of microstates unavailable to larger nanoparticles but in which the small fluorescent molecules may reside[9]. In an attempt to circumvent the complication of DNA origami when using DNA self-assembly to orient fluorescent molecules, embedding the dye molecules into a simpler four-arm junction (4AJ) structure could reduce the possible folding pathways and may result in a higher precision of molecule orientation[10]. Ensemble optical measurements of such structures suggest orientational control of embedded dyes within an aggregate of multiple dyes over the population of structures[11-13]. Single molecule studies of structures comprising such populations would give further insight into the precision of orientational control that can be achieved for conjugated molecules within DNA nanostructures.

A fixed dipole above a dielectric interface produces a unique point spread function (PSF) depending on its orientation[14-16]. Fitting these PSFs with analysis software allows one to infer the orientation parameters of its single dye molecule source[17-19]. To correlate the dipole orientation to the DNA on which it is bound, super-resolution microscopy (SRM) using DNA-PAINT may be employed to resolve specific locations on the DNA structure[20]. By creating an asymmetric pattern of docking sites to resolve in SRM, the azimuthal orientation and face-up/face-down state of the DNA structure may be determined[7]. DNA origami serves as a suitable substrate for immobilizing 4AJs and hosting an asymmetric pattern of SRM docking sites[21]. In this work, we attempt to determine to what precision a single two-tether cyanine 5 (Cy5) molecule embedded in a component strand of a 4AJ may be oriented in a population.

3.3 Results and Discussion

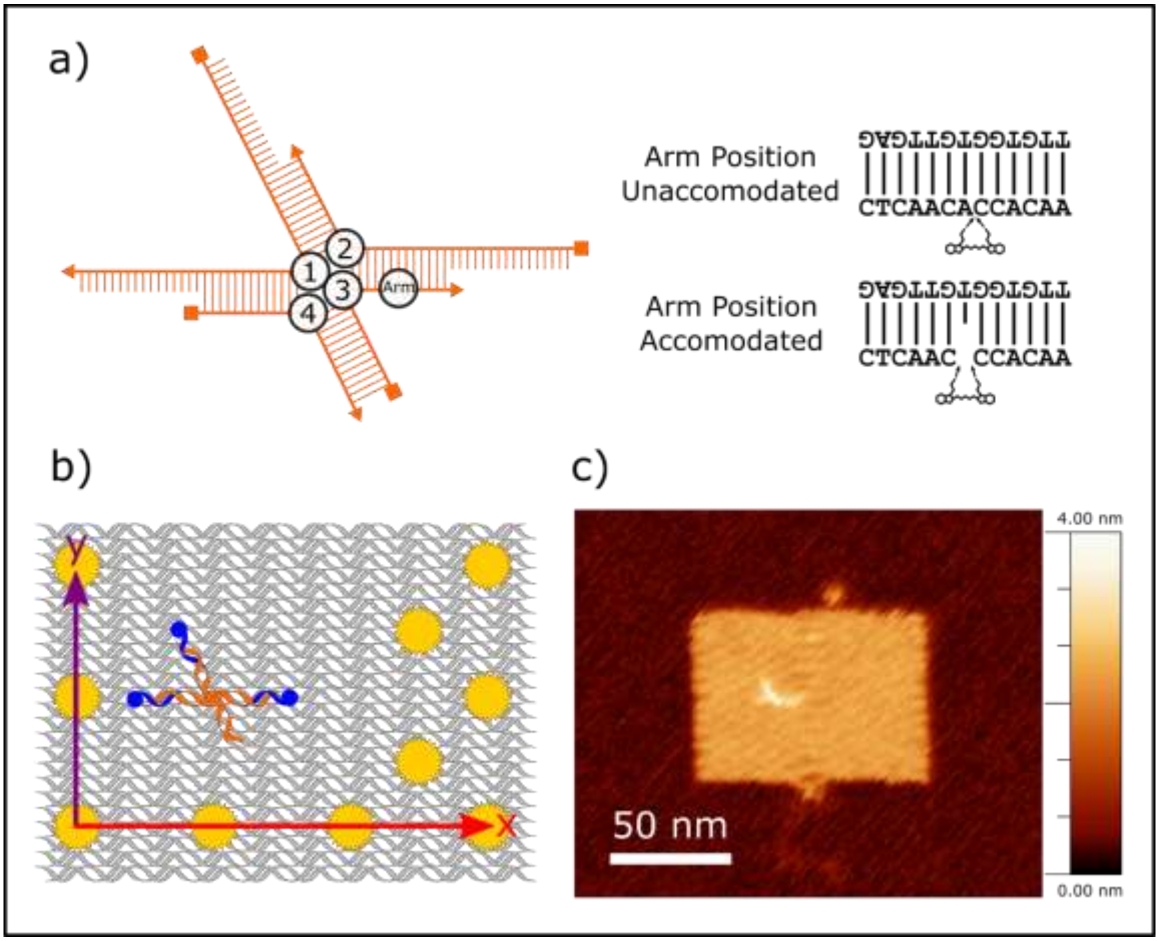

Figure 3.1: a) A diagram of the staple routing of the 4AJ with the positions of the individual Cy5 locations in the junction and in the arm indicated by black circles. The local sequence variants of the Arm position are given to the right. b) A diagram showing the design of the rectangular DNA origami template (gray helices) that serves as the primary substrate for isolating sm Cy5 molecules on 4AJs. The blue circles/helices indicate the extended staple strand sticky-end locations on the origami, which are complementary to ssDNA extensions on three of the four arms of the 4AJ (orange strands). The gold starbursts indicate the locations of the extended origami staples that serve as docking sites complementary to Cy3b labeled imager strands used in SRM. The asymmetric pattern of docking sites allows for the determination of the absolute orientation of each origami structure, and this orientation determines the XYZ axes of the DNA substrate on which a 4AJ is anchored. c) AFM image confirming the 4AJs bind to the rectangular origami structures in the designed location and configuration.

To isolate single 4AJs, the constructs were assembled and PAGE purified separate from the DNA origami tiles and then mixed with origami in a 2:1 4AJ:origami ratio. This ensured that only properly formed 4AJ structures were present in the sample and reduced the background signal from unbound 4AJs during sm dipole imaging. The 4AJs were formed from four unique sequences to increase stability with three “sticky-end” extensions to allow the 4AJ to be immobilized onto origami at three points. Six versions of 4AJ were studied, each with a two-tether Cy5 monomer embedded into one of the component strands. As illustrated in Figure 3.1a, four of the six structures positioned the Cy5 at the site of the junction, one on each of the component sequences. The remaining two structures placed the Cy5 in one arm of the 4AJ, in either a sequence where a base was omitted to accommodate the Cy5 molecule or a fully complementary sequence where the Cy5 was unaccommodated (Table 3.1). Studies into the structure of 4AJs suggest that the preferred configuration is of a stacked X shape rather than a two-dimensional equiangular cross[22]. The three anchor points extended from the DNA origami substrate were chosen to match this preferred configuration. Figure 3.1b shows the design of the rectangular DNA origami tile substrate used for this study. The 4AJ is immobilized on the tile via three extended staple strands within the tile complementary to specific sticky-ends on the 4AJ. Surrounding the 4AJ location is an asymmetric pattern of extended sticky-end docking sites complementary to the short ssDNA imager strands functionalized with Cy3b used in SRM via DNA-PAINT. Atomic force microscopy (AFM) images confirmed the presence of 4AJs on the origami tiles after mixing, as seen in Figure 3.1c.

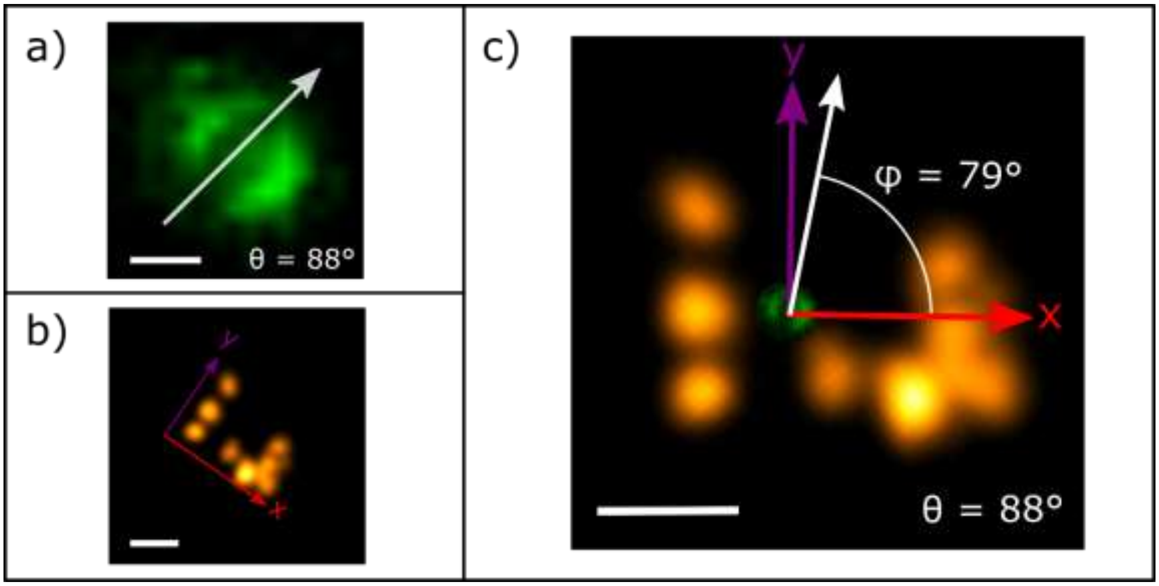

Figure 3.2: The correlation of measured dipole angles to their DNA substrate. a) The observed dipole PSF pattern with the calculated azimuthal angle, ~45°, overlaid with a white arrow. The extracted polar angle θ is near parallel with the substrate. b) the SRM pattern observed at the center of a). The observed origami substrate is present in the face-up orientation. Measurement of the origami orientation, represented as the red x-axis, is 325° ± 13°. Correlated dipole angles are reported relative to the measured x-axis orientation of their DNA substrate. c) Calculation of the relative dipole angles shown in the overlaid image. The dipole pattern has been scaled down for illustrative purposes. Scale bars: 500 nm at 400 nm defocus for a, 500 nm for c, 50 nm for b.

Defocused dipole PSF and SRM images of the same sample region were collected using total internal reflectance microscopy and correlated using silanated gold nanoparticles distributed randomly in the field of view and visible in each image channel (Figure 3.6). Cy5 dipole emissions from isolated origami were analyzed using dipole fitting software to extract their polar (θ) and azimuthal (ϕ) angles[17]. Figure 3.2a shows the computed angles for a single dipole. Figure 3.2b shows a SRM image of the DNA origami substrate under the 4AJ. The three docking sites on each edge of the short axis are located on either end of their respective helical domains, which run along the long axis of the rectangular tile. We measure the angle of these helical domains from localizations in SRM. Two arms of the 4AJ are anchored to a single helical domain so the measured angle of the origami defines as the x-axis of the origami substrate and an axis of the 4AJ (Figure 3.1b). The y-axis points to the long edge of the tile with no localizations. Correlating the dipole orientation with the DNA substrate is achieved by normalizing the dipole angles to the origami coordinate system as shown in Figure 3.2c.

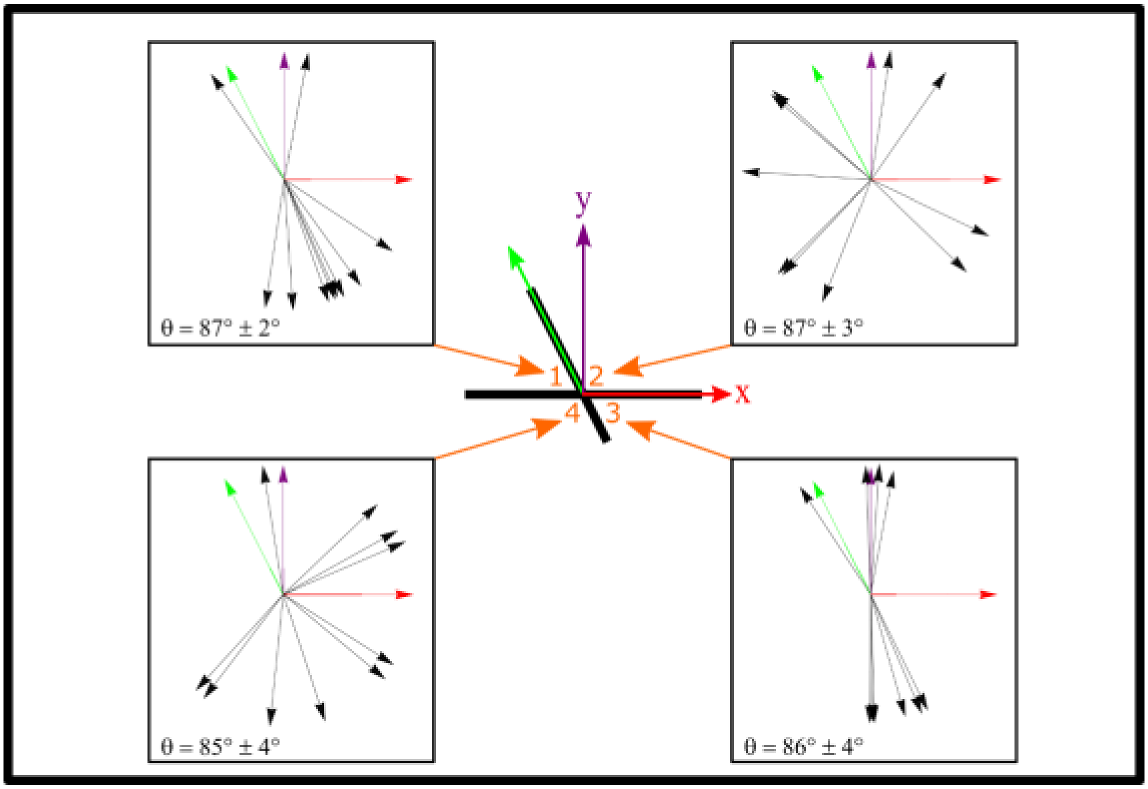

Figure 3.3: The correlated azimuthal (ϕ) and average polar (θ) angles for each Cy5 monomer located at the cross-over of a 4AJ structure. The orange location numbers correspond to the 4AJ component ssDNA strand with the Cy5 modification and shows where the Cy5 located within the cross-over. The XY orientation of the 4AJ shown in red (x) and purple (y) corresponds directly to the XY coordinate system established by the rectangular origami substrate. The angle of the off-axis (green arrow) helical domain was determined by AFM to be 117°. When the Cy5 molecules are placed in the 1 and 3 locations the resulting azimuthal angles tend to prefer an orientation parallel or anti-parallel to this off-angle.

Across all structures measured with the Cy5 molecule placed in the junction of the 4AJ, the dipoles preferred a polar orientation nearly parallel with the sample surface.

Average measured polar angles for each of these dye positions, shown in Figure 3.3, ranged from 85° ± 4° to 87° ± 2°. These values are close to the preferred polar orientation for unbound Cy5 molecules at a glass interface and may suggest that the junction allows enough freedom for the dye to orient itself[23]. Such freedom may be expected for the junction since thermodynamic calculations indicate high probabilities for the bases in the junction to be unpaired at equilibrium (Figures 3.7, 3.8). Further evidence that Cy5 molecules can orient freely within the junction comes from the distribution of measured azimuthal (ϕ) angles for each dye location, particularly when the dye molecules are in locations 2 and 4. The measured azimuthal angles suggest a more restricted freedom of orientation for dyes in position 1 or 3.The dyes in either of these positions also appear to prefer an orientation near the off-angle helical domain determined by AFM analysis. Due to the symmetry of the dipole PSF, emission patterns from azimuthal angles of ϕ and ϕ + 180° are very similar when the polar angle is close to 90°. For this reason, we assume that either azimuthal angle is valid for such a pattern. In the best-case scenario, that is, the smallest possible distribution of relative orientations, the dispersions in the azimuthal angles of positions 1 and 3 are 21° and 15° respectively. Dyes in positions 2 and 4 have no apparent azimuthal preference. Note, based on the apparent structure of the dipole PSF images, we do not expect the dyes to be rotating freely during the 300 ms integration time. Rather, we believe the dyes may rotate freely within the structures but stabilize in a fixed orientation once immobilized. In any case, positioning dyes in the inner locations of the junction (1 and 3) might provide the best possibility for high orientational precision within a 4AJ.

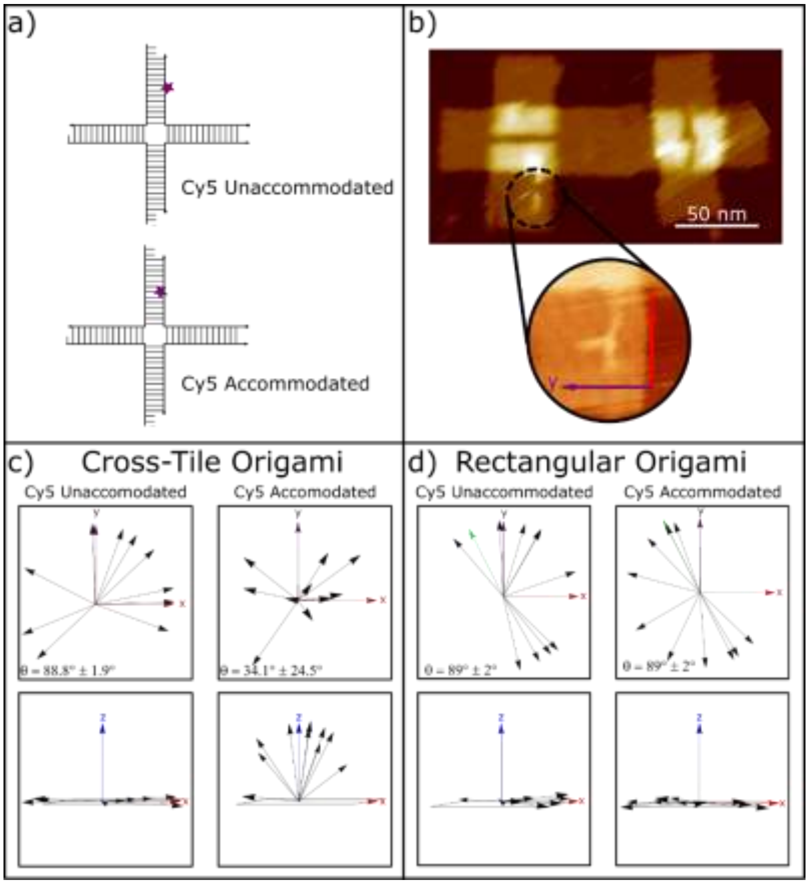

Figure 3.4: The measured orientations of dipoles within the dsDNA domain of an arm of a 4AJ anchored on both a rectangular origami and a cross-tile dimer[7]. a) The schematic of a 4AJ with a Cy5 embedded in one arm in either an unaccommodated or accommodated sequence. The omitted base in the accommodated sequence is intended to allow the Cy5 molecule room to settle into the helix. b) AFM image of an origami cross-tile dimer with an anchored 4AJ. The magnified area of the origami shows the 4AJ anchored in an equiangular cross configuration consistent with the anchor locations chosen for the cross-tile origami substrate. The 4AJs anchored on cross-tiles are identical to those anchored to rectangular origami. c) Dipoles measured relative to 4AJs anchored to cross-tile origami substrates present in predominately a face-down orientation. While azimuthal angles remain dispersed among the observed structures, the polar angles (θ) of accommodated Cy5 molecules show some restriction in their allowed orientation. d) The Cy5 dipoles measured relative to 4AJs anchored to rectangular origami structures were measured in the face-up orientation. The polar angles for each of the accommodated and unaccommodated Cy5 dyes tend toward parallel with the glass surface and the azimuthal (ϕ) angles measured do not show any preference toward a single orientation.

Dyes were placed in an arm of the 4AJ in the middle of the dsDNA helix to compare to previous work on dye orientations embedded directly into the double helix of an origami cross-tile dimer structure[7]. Figure 3.4 shows the distribution of dipoles measured in the arm of a 4AJ anchored to two different origami substrates, a cross-tile dimer (Figure 3.4c) and a rectangular origami structure (Figure 3.4d). The same 4AJ constructs were anchored on rectangular origami and cross-tile origami structures, and while the anchor pattern differed between the rectangle and cross-tile origami, the arm of the 4AJ in which the dyes were embedded runs parallel to the substrate helical domain in each structure. The reason for using two separate substrates is that while the rectangular origami is observed on the surface in a face-up orientation more often than face-down, the opposite is true for the cross-tile dimers, which are most often observed in the face-down orientation. This behavior allows for easy comparison of dipole orientations between similar structures when the dye molecule is within DNA directly on the glass surface versus DNA that is away from the glass surface. While the resulting measured orientations in unaccommodated dye molecules do not differ in a significant way between the face-up and face-down substrates, the same cannot be said for accommodated dyes. The removal of a base adjacent to the dye in the sequence is made to accommodate the Cy5 molecule in the helix. While there was no a noticeable difference in measured orientations of accommodated versus unaccommodated dyes in face-up substrates, a considerable difference in the average polar angle as well as a large dispersion was observed in the dyes on face-down substrates at 34° ± 25°. The greater variance in face-down dye orientations may reflect a greater influence of the surface and surface charge on the local orientations of immobilized dyes.

3.4 Conclusions

The dipole orientations of Cy5 molecules in 4AJs in both the junction and in the dsDNA domain of one of the arms were measured relative to the orientation of the DNA in which they were embedded. As in previous measurements of dipoles relative to their DNA substrates, the observed polar angles (θ) for most structures possessed a tight distribution, while azimuthal (ϕ) angles presented with a large dispersion in all but two structures. The observed polar angles for all but the accommodated Cy5 molecules in 4AJs on face-down substrates agreed with polar orientations of unbound Cy5 molecules on a glass surface suggesting the 4AJ substrate provides the dye with significant freedom of movement in most cases. The relatively open structure of the underlying origami weave may further enable influence from the substrate on dye orientation. The 4AJs on face-down substrates appear to limit the freedom of orientation of Cy5 molecules to a certain degree as the average polar angle was not near parallel to the surface and possessed a larger dispersion of angles compared to those observed in any other structure. The distribution of azimuthal angles within most structures also suggests a large freedom of movement of Cy5 molecules within 4AJs with the notable exception of those molecules located within the center of the junction. These molecules appear to prefer an azimuthal orientation that coincides with the angle of one of the helices of the 4AJ in the stacked X configuration. While ensemble optical measurements of dye molecules positioned with DNA show certain orientational properties across a population, single-molecule super-resolution measurements of individual structures show a wide dispersion in the orientations of single dye molecules by both relatively simple and by more complex DNA structures. These results provide insight into the control of molecular orientations using DNA self-assembly and provide an avenue for characterization of future DNA-templated molecular assemblies.

3.5 Acknowledgments

We thank members of the Nanoscale Materials and Device group for valuable assistance and discussions, particularly Natalya Hallstrom, George Dickinson, and Christopher Green. The optical microscope used in this work was jointly paid for by the National Science Foundation (grant 1807809), the Semiconductor Research Corporation (contract 2842.001), and the Idaho Global Entrepreneurial Mission. Select oligos, optical components, and chemicals used in this work were paid for by the National Science Foundation (grant 1648655).

3.6 References

1 Feynman, R. P. There's plenty of room at the bottom. California Institute of Technology, Engineering and Science magazine (1960).

2 Seeman, N. C. & Sleiman, H. F. DNA nanotechnology. Nature Reviews Materials 3, 17068 (2018).

3 Ke, Y., Castro, C. & Choi, J. H. Structural DNA nanotechnology: artificial nanostructures for biomedical research. Annual review of biomedical engineering 20, 375-401 (2018).

4 Hübner, K. et al. Directing Single-Molecule Emission with DNA Origami-Assembled Optical Antennas. Nano Letters 19, 6629-6634, doi:10.1021/acs.nanolett.9b02886 (2019).

5 Kroutil, O. e., Romancová, I., Sip, M. & Chval, Z. k. Cy3 and Cy5 dyes terminally attached to 5′ C end of DNA: structure, dynamics, and energetics. The Journal of Physical Chemistry B 118, 13564-13572 (2014).

6 Boulais, É. et al. Programmed coherent coupling in a synthetic DNA-based excitonic circuit. Nature materials 17, 159-166 (2018).

7 Ward, B. M. In Preparation.

8 Lee Tin Wah, J., David, C., Rudiuk, S., Baigl, D. & Estevez-Torres, A. Observing and Controlling the Folding Pathway of DNA Origami at the Nanoscale. ACS Nano 10, 1978-1987, doi:10.1021/acsnano.5b05972 (2016).

9 Wagenbauer, K. F., Wachauf, C. H. & Dietz, H. Quantifying quality in DNA self-assembly. Nature Communications 5, 3691, doi:10.1038/ncomms4691 (2014).

10 Joo, C., McKinney, S. A., Lilley, D. M. & Ha, T. Exploring rare conformational species and ionic effects in DNA Holliday junctions using single-molecule spectroscopy. Journal of molecular biology 341, 739-751 (2004).

11 Cannon, B. L. et al. Large Davydov Splitting and Strong Fluorescence Suppression: An Investigation of Exciton Delocalization in DNA-Templated Holliday Junction Dye Aggregates. The Journal of Physical Chemistry A 122, 2086-2095, doi:10.1021/acs.jpca.7b12668 (2018).

12 Heussman, D. et al. Measuring local conformations and conformational disorder of (Cy3) 2 dimer labeled DNA fork junctions using absorbance, circular dichroism and two-dimensional fluorescence spectroscopy. Faraday Discussions (2019).

13 Kringle, L. et al. Temperature-dependent conformations of exciton-coupled Cy3 dimers in double-stranded DNA. The Journal of chemical physics 148, 085101 (2018).

14 Bartko, A. P. & Dickson, R. M. Imaging three-dimensional single molecule orientations. The Journal of Physical Chemistry B 103, 11237-11241 (1999).

15 Lieb, M. A., Zavislan, J. M. & Novotny, L. Single-molecule orientations determined by direct emission pattern imaging. Journal of the Optical Society of America B 21, 1210-1215, doi:10.1364/JOSAB.21.001210 (2004).

16 in Principles of Nano-Optics (eds Bert Hecht & Lukas Novotny) 313-337 (Cambridge University Press, 2012).

17 Aguet, F., Geissbühler, S., Märki, I., Lasser, T. & Unser, M. Super-resolution orientation estimation and localization of fluorescent dipoles using 3-D steerable filters. Optics Express 17, 6829-6848, doi:10.1364/OE.17.006829 (2009).

18 Mortensen, K. I., Sung, J., Flyvbjerg, H. & Spudich, J. A. Optimized measurements of separations and angles between intra-molecular fluorescent markers. Nature communications 6, 8621 (2015).

19 Patra, D., Gregor, I. & Enderlein, J. Image Analysis of Defocused Single-Molecule Images for Three-Dimensional Molecule Orientation Studies. The Journal of Physical Chemistry A 108, 6836-6841, doi:10.1021/jp048188m (2004).

20 Jungmann, R. et al. Multiplexed 3D cellular super-resolution imaging with DNA-PAINT and Exchange-PAINT. Nature methods 11, 313 (2014).

21 Fan, S. et al. Create Nanoscale Patterns with DNA Origami. Small 15, 1805554 (2019).

22 Eichman, B. F., Vargason, J. M., Mooers, B. H. M. & Ho, P. S. The Holliday junction in an inverted repeat DNA sequence: Sequence effects on the structure of four-way junctions. Proceedings of the National Academy of Sciences 97, 3971, doi:10.1073/pnas.97.8.3971 (2000).

23 Böhmer, M. & Enderlein, J. Orientation imaging of single molecules by wide-field epifluorescence microscopy. JOSA B 20, 554-559 (2003).

3.7 Supplementary Information

3.7.1 Methods

3.7.1.1 DNA Synthesis

The six different four arm junctions (4AJs) were mixed and purified individually. Each 4AJ is comprised of four unique component ssDNA strands with one of the component strands containing an internal Cy5 modification. The sequences of the component strands can be found in Table 3.1. The unaccommodated and accommodated Cy5 4AJs contain a version of the 4AJ3 sequence with the internal Cy5 located away from the cross-over and in an anchored arm of the 4AJ. All 4AJs contain three non-dye functionalized ssDNA strands and one Cy5 modified strand. 4AJs were prepared by mixing the four separate strand components of each junction at a 1:1:1:1 ratio in a 1X TAE, 12.5 mM $MgCl_2$ solution. The solutions were covered with foil and annealed for 12 hours at room temperature. A ficoll/bromophenol blue loading buffer was mixed with the junctions in a 1:4 ratio respectively. Solutions were pipetted into gels and run with a 1X TAE, 12.5 mM $MgCl_2$ buffer at 120 V at 20 ºC for 2 hours under foil. 4AJs were purified using polyacrylamide gel electrophoresis (PAGE). 12% polyacrylamide gels were created with a final buffer of nominal 1X TAE, 12.5 mM $MgCl_2$ concentrations. Bands were then imaged and extracted from the gel. Bands were placed in Eppendorf tubes with 0.5X TBE, 15 mM $MgCl_2$ buffer and pulverized to elute for 12 hours. After centrifuging at 12000 rcf for 3 minutes, supernatant from tubes was extracted and placed into smaller Eppendorf tubes. The stock concentrations were then diluted to working concentrations.

DNA origami rectangles where annealed in a solution of 1:10:50:10 scaffold strands (Bayou BioLabs) to body staple to docking staple to anchor staple (Integrated

DNA Technologies) ratio in a 0.5X TAE buffer containing 18 mM $MgCl_2$. Oligos and scaffold strand were purchased with standard desalting and used as received. The annealed solution was purified in a 0.8% agarose gel prepared with 0.5X TAE, 8 mM $MgCl_2$. 4AJs were anchored to the rectangular origami by mixing the purified origami solution with the desired 4AJ in a ratio of 1:2 origami to 4AJ structures and annealed at RT for at least 24 hours prior to imaging.

The DNA origami A and B cross-tiles where folded separately by annealing a solution of 1:5:10 scaffold strands to body staples to edge in a 0.5X TBE buffer containing 12.5 mM $MgCl_2$[1,2]. The internal staple strand anchor modifications were made on the A tile only at a 10:1 anchor to scaffold ratio. Annealed solutions where purified via gel electrophoresis in a 0.8% agarose gel prepared with 0.5X TBE, 8 mM $MgCl_2$. 4AJ DNA origami dimers where formed by mixing a 1:1:2 ratio of A:B:4AJs in a 0.5X TBE buffer with 15 mM $MgCl_2$ and incubated at ambient temperature for at least 24 hours before imaging. All solutions were stored in a dark environment when not being measured.

3.7.1.2 Sample Preparation

Glass coverslips were functionalized on one side with 150 nm silane gold nanoparticles (NanoPartz) for drift correction when processing SRM image stacks and to perform image registration across multiple channels[3]. Glass cover slips were prepared for DNA-PAINT super-resolution microscopy using a method to be published and then assembled into Luer channel microscope slide[3]. 200 µL of 5 pM DNA origami solution was pushed into the channel and left to anneal at RT for 10 minutes. The channel was then rinsed with 1 mL of 0.5X TBE buffer with 15 mM $MgCl_2$ before imaging.

3.7.1.3 Dipole Imaging

Single molecule (sm) dipole imaging was carried out on a Nikon Eclipse T*i*2 inverted microscope with a Nikon CFI Apochromat TIRF 100x oil immersion objective (NA = 1.49). All excitation wavelengths used in imaging are sourced from a Nikon Laser Univ model LUN-F. Sharp focus of the surface was found using the gold nanoparticles excited at 488 nm to avoid photobleaching the Cy5 molecules. The stage was then stepped toward the objective 400 nm using the built-in piezo movement controls for defocused imaging. Cy5 molecules were excited at 640 nm in total internal reflection fluorescence (TIRF) mode. A quad band excitation filter and beam splitter was used to clean up the excitation source and a quad band emission filter isolated the emission from Cy5 molecules, which was then collected by a Princeton Instruments ProEM HS: 512B-N EMCCD with an EM gain of 100X. The integration time for each captured frame was 250 ms.

3.7.1.4 Super-Resolution Imaging

Immediately following single molecule dipole imaging, the optical system was reconfigured to image Cy3b fluorophores for PAINT super-resolution microscopy (SRM) of the same area with TIRF illumination[4]. The imaging buffer was exchanged with a 0.5X TBE solution with 35 mM $MgCl_2$ and 3 nM Imager Strand while on the microscope. The imager strand sequence is given in Table 3.2. All SRM was performed at 150 ms/frame for 10,000 frames with an EM gain of 100X.

3.7.1.5 Image Processing

Individual frames of defocused sm-dipole PSFs were analyzed using the steerableDipoleDetector MATLAB algorithm to extract the orientation components[5]. SRM image stacks were analyzed using the THUNDERSTORM ImageJ plug-in[6]. The two channels were registered using the gold nanoparticles randomly distributed across the field of view as registration marks to create a master image. From the master image, dipole orientations confirmed to originate from a single DNA origami substrate were compared to the measured orientation of that DNA structure. The number of individual constructs analyzed, *n*, for all structures was 10.

3.7.2 Supplementary Figures

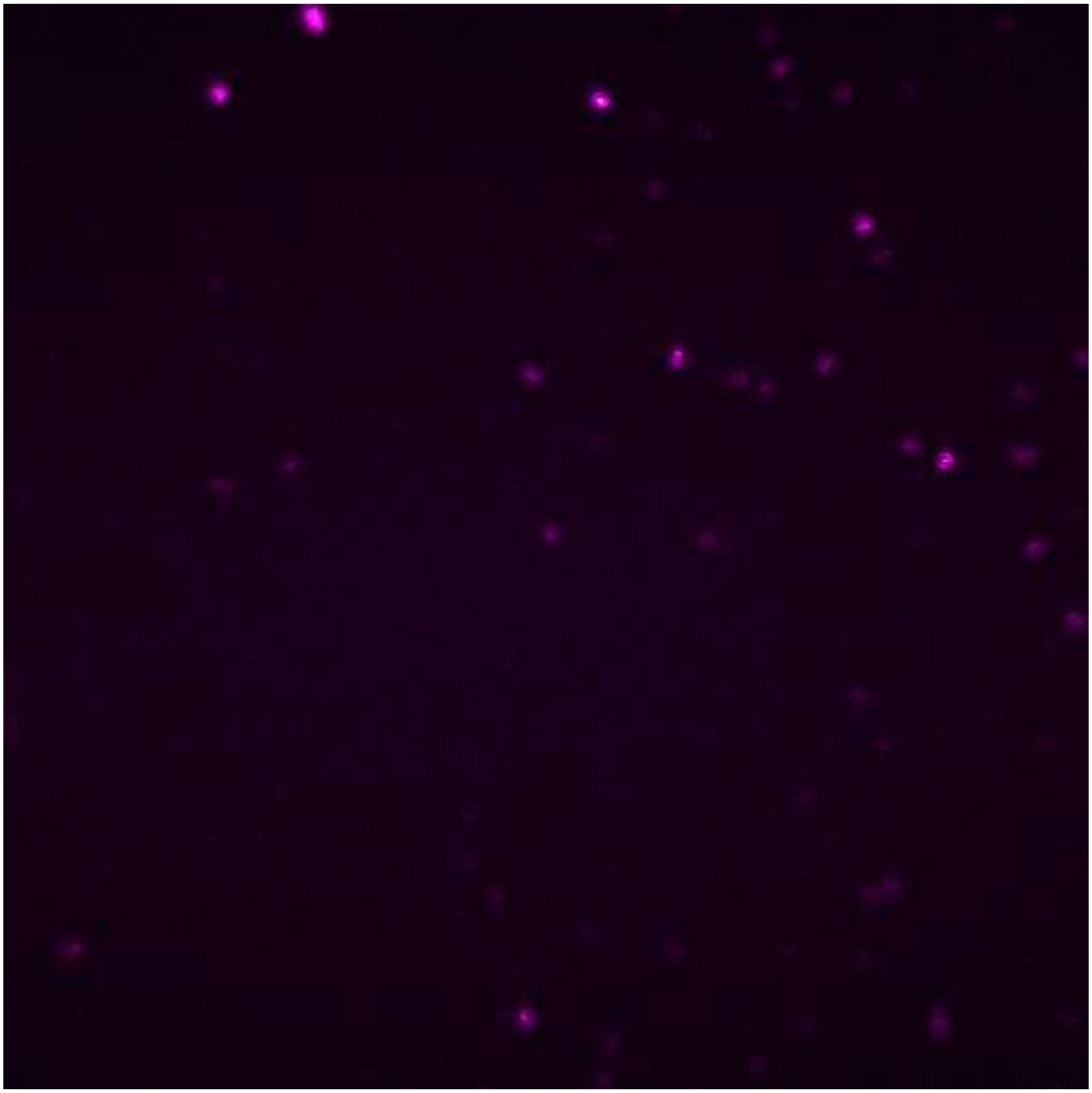

Figure 3.5: A defocused image of Cy5 dipoles embedded on 4AJs anchored to DNA origami. The distinctive two-lobed patterns are characteristic PSFs of dipoles laying parallel to the glass interface. Scattering from gold nanoparticles is also present in the image.

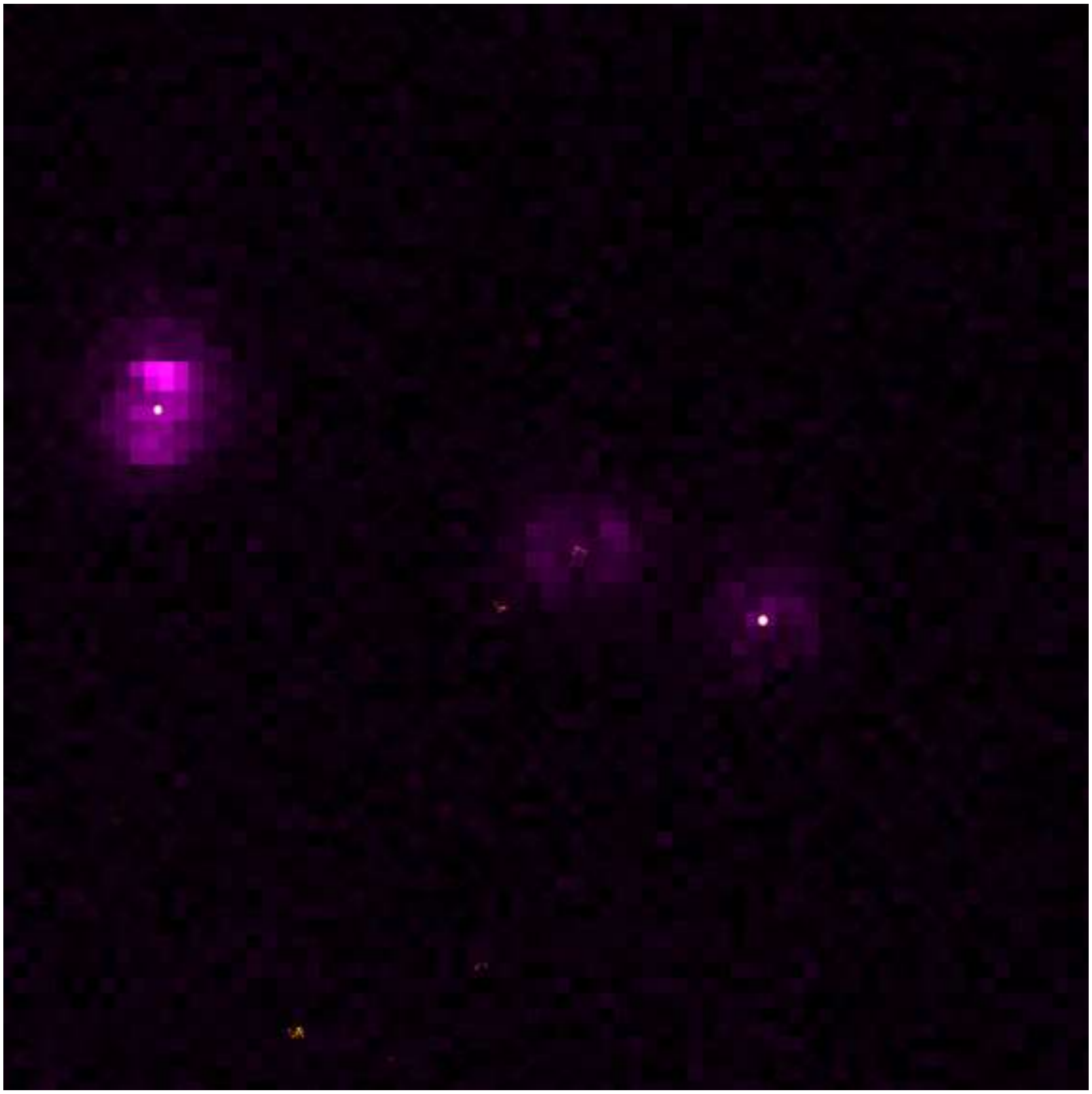

Figure 3.6 A region of a correlated Cy5 dipole emission and SRM image showing signals from gold nanoparticles (bright circles in SRM) in each channel. The center of the image shows a Cy5 dipole emission pattern with a rectangular origami tile in the center. Three other origami structures are visible in the image without Cy5 emission patterns.

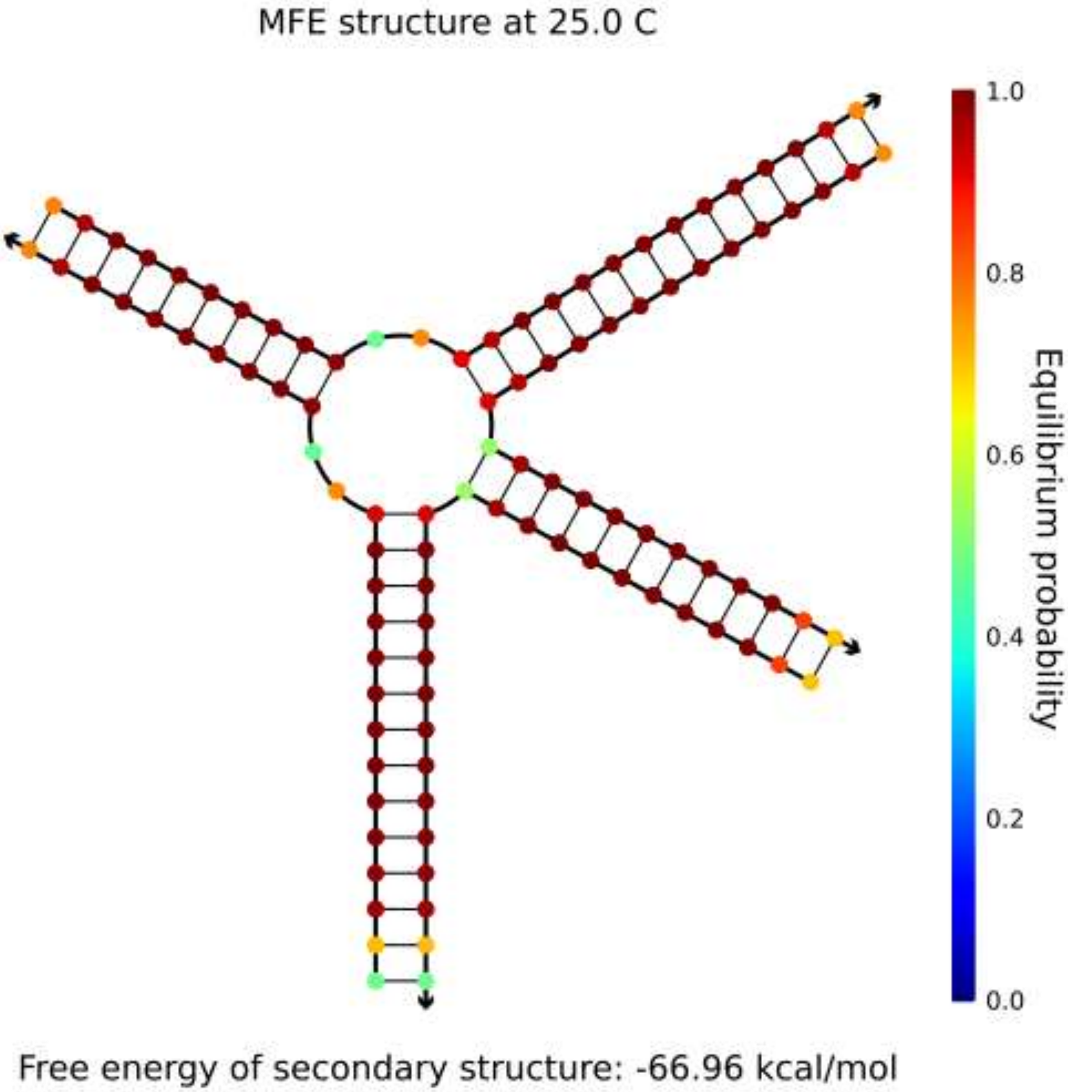

Figure 3.7 The equilibrium probability of the base pairing of the 4AJ calculated using NUPACK[7]. The bases near the junction have a lower probability of being paired at 25 ºC compared to the rest of the 4AJ.

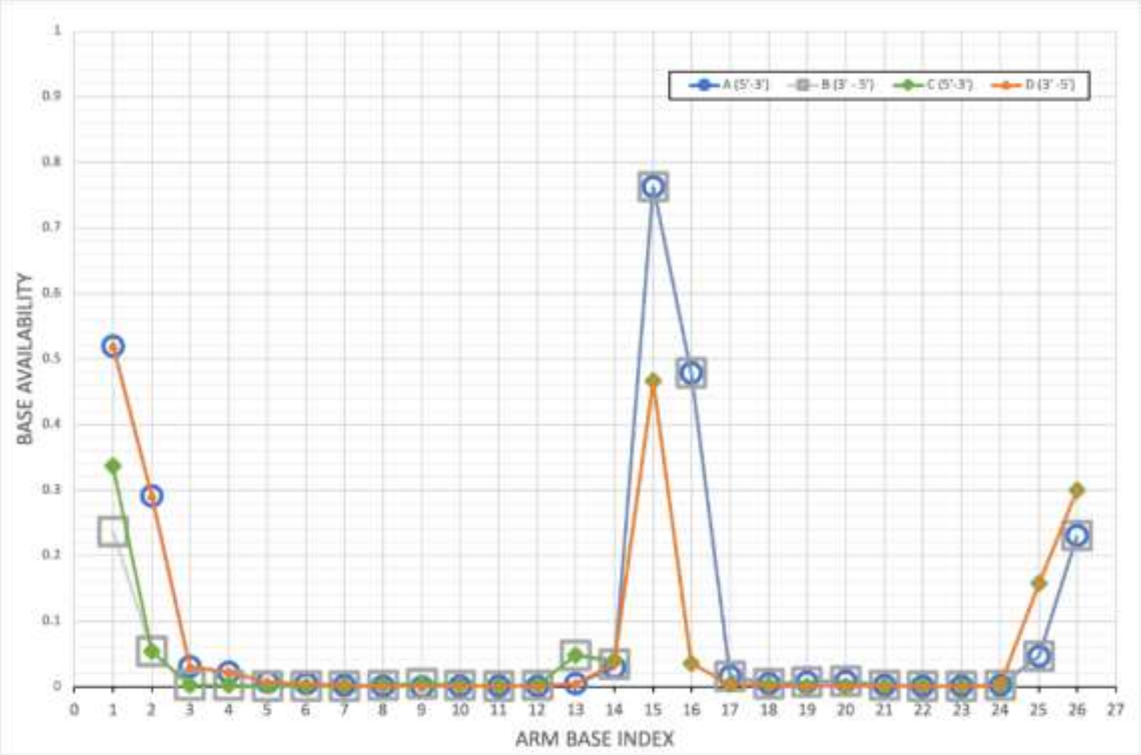

Figure 3.8 The base availability graph of each of the four component strands in the 4AJ[7]. The peak in availability occurs at the junctions showing a loss of base pair stability in that area.

3.7.3 Supplementary Tables

Table 3.1: The component sequences of the 4AJ

Name	Sequence	Notes
4AJ-Cy5	CGTAGGAGCACTGGTTATATAATCGCTCG/iCy5/CATATTATGACTGTCGTAGGCGGTAGAGA	
4AJ2-Cy5	AGGAAGATACTGTTGTTTGTGGTGTTGAG/iCy5/CGAGCGATTATAT	
4AJ3-Cy5	CACTCACATTCCA/iCy5/CTCAACACCACAA	
4AJ4-Cy5	CAGTCATAATATG/iCy5/TGGAATGTGAGTG	
4AJ1	CGTAGGAGCACTGGTTATATAATCGCTCGCATATTATGACTGTCGTAGGCGGTAGAGA	
4AJ2	AGGAAGATACTGTTGTTTGTGGTGTTGAGCGAGCGATTATAT	
4AJ3	CACTCACATTCCACTCAACACCACAA	
4AJ4	CAGTCATAATATGTGGAATGTGAGTG	
4AJ3-Cy5ArmU	CACTCACATTCCACTCAAC/iCy5/ACCACAA	Unaccommodated Cy5
4AJ3-Cy5ArmA	CACTCACATTCCACTCAAC/iCy5/CCACAA	Accommodated Cy5

Table 3.2 Imager Strand Sequence and Docking Site staple extension for SRM

Name	Sequence	Notes
Imager Strand	CTAGATGTAT/Cy3b/	
Docking Site Staple 3’ Extension	ATACATCT	

3.7.4 Supplementary References

1 Green, C. M. et al. Metrology of DNA arrays by super-resolution microscopy. Nanoscale 9, 10205-10211, doi:10.1039/C7NR00928C (2017).

2 Liu, W., Zhong, H., Wang, R. & Seeman, N. C. Crystalline Two-Dimensional DNA-Origami Arrays. Angewandte Chemie International Edition 50, 264-267, doi:10.1002/anie.201005911 (2011).

3 Green, C. M. In preparation.

4 Jungmann, R. et al. Multiplexed 3D cellular super-resolution imaging with DNA-PAINT and Exchange-PAINT. Nature methods 11, 313 (2014).

5 Aguet, F., Geissbühler, S., Märki, I., Lasser, T. & Unser, M. Super-resolution orientation estimation and localization of fluorescent dipoles using 3-D steerable filters. Optics Express 17, 6829-6848, doi:10.1364/OE.17.006829 (2009).

6 Ovesný, M., Křížek, P., Borkovec, J., Švindrych, Z. & Hagen, G. M. ThunderSTORM: a comprehensive ImageJ plug-in for PALM and STORM data analysis and super-resolution imaging. Bioinformatics 30, 2389-2390 (2014).

7 Zadeh, J. N. et al. NUPACK: analysis and design of nucleic acid systems. Journal of computational chemistry 32, 170-173 (2011).

CHAPTER FOUR: CONCLUSIONS

In conclusion, the orientations of 212 individual fluorescent dye molecules were measured relative to the orientations of the DNA origami substrates to which they were bound. These measurements represent, to the best of our knowledge, the first instances of correlated single-molecule dipole imaging and super-resolution microscopy using the protocols established herein. This smSRM method was successfully executed on two separate but similar microscopes giving us confidence in the viability of the technique.

The double helix of DNA origami can orient several different dye molecule species with a consistent polar angle and this preferred polar (θ) angle has a dependence on the location within the twist of the helix. Conversely, dyes embedded in an immobile four-arm junction at either the junction or within an arm have the freedom to orient themselves to the preferred polar angle of free dyes on a glass surface in most configurations. The control over the azimuthal (ϕ) orientation of fluorescent dyes by any of the DNA substrates studied is far less precise. Of the systems studied, none appear to orient dipoles in a preferred azimuthal angle with the notable exception of the acute angle locations of the four-arm junction, where the measured dipoles appear to prefer to align themselves with the off-angle helical domain. In general, single molecule measurements show low precision in the orientation control of fluorescent molecule monomers by DNA nanostructures.

Future work to further investigate and improve the orientational control of DNA nanostructures should include a study on effects of the concentration and type of buffer salt on relative dipole orientations. Hydrostatic repulsion of DNA sugar-phosphate backbones is sensitive to cation concentrations and minor changes in salt could have major implications on local energy landscapes. Examining the effects of proximal bases and/or the inclusion of LNA bases in the sequence on dipole orientation precision may lead to approaches to reduce dipole orientation dispersion across a population.

While the control of fluorescent dye monomers is important for many optical systems, the orientation of dyes within an aggregate relative to each other and to the DNA substrate is of particular interest in systems exhibiting coherent coupling. Investigating the orientations of dyes within these multi-dye aggregate systems using this sm microscopy technique is an important next step but will require intense study into controlling the photobleaching of dyes with techniques such as introducing triplet state quenching buffers and oxygen scavengers since strongly-coupled aggregates have significantly suppressed fluorescence emission and thus require longer imaging times. Studying such systems could provide further insight into whether the DNA substrate or proximal dyes have a greater influence over the orientations of dyes within an aggregate. This information will be critical for future molecular quantum computing devices.